ISSN 1674-1056
http://cpb.iphy.ac.cn
http://iopscience.iop.org/cpb
中国物理 B
Chinese Physics
中国物理 Chinese Physics B

Topology of triple-point metals

Georg W. Winkler, Sobhit Singh, Alexey A. Soluyanov

Citation: Chin. Phys. B . 2019, 28(7): 077303. **doi:** 10.1088/1674-1056/28/7/077303
Journal homepage: http://cpb.iphy.ac.cn; http://iopscience.iop.org/cpb

What follows is a list of articles you may be interested in

Double band-inversions of bilayer phosphorene under strain and their effects on optical absorption

Shi He(何诗), Mou Yang(杨谋), Rui-Qiang Wang(王瑞强)
Chin. Phys. B . 2018, 27(4): 047303. **doi:** 10.1088/1674-1056/27/4/047303

Conductivity and band alignment of $LaCrO_3/SrTiO_3$ (111) heterostructure

Yan-Peng Hong(洪彦鹏), Xin-Xin Wang(王欣欣), Guo-Liang Qu(曲国良), Cheng-Jian Li(厉承剑), Hong-Xia Xue(薛红霞), Ke-Jian Liu(刘科践), Yong-Chun Li(李永春), Chang-Min Xiong(熊昌民), Rui-Fen Dou(窦瑞芬), Lin He(何林), Jia-Cai Nie(聂家财)
Chin. Phys. B . 2018, 27(4): 047301. **doi:** 10.1088/1674-1056/27/4/047301

Electronic structure of silicene

L. C. Lew Yan Voon
Chin. Phys. B . 2015, 24(8): 087309. **doi:** 10.1088/1674-1056/24/8/087309

Comparison of electronic structure between monolayer silicenes on Ag (111)

Chun-Liang Lin, Ryuichi Arafune, Maki Kawai, Noriaki Takagi
Chin. Phys. B . 2015, 24(8): 087307. **doi:** 10.1088/1674-1056/24/8/087307

Two-dimensional metallic behavior at polar $MgO/BaTiO_3$ (110) interfaces

Du Yan-Ling, Wang Chun-Lei, Li Ji-Chao, Zhang Xin-Hua, Wang Fu-Ning, Liu Jian, Zhu Yuan-Hu, Yin Na, Mei Liang-Mo
Chin. Phys. B . 2015, 24(3): 037301. **doi:** 10.1088/1674-1056/24/3/037301

TOPICAL REVIEW — Topological semimetals

Topology of triple-point metals*

Georg W. Winkler[1], Sobhit Singh[2], and Alexey A. Soluyanov[3,4,†]

[1] Microsoft Quantum, Microsoft Station Q, University of California, Santa Barbara, California 93106-6105, USA
[2] Department of Physics and Astronomy, Rutgers University, Piscataway, New Jersey 08854, USA
[3] Institute of Physics, University of Zurich, Winterthurerstrasse 190, 8057 Zurich, Switzerland
[4] Department of Physics, St. Petersburg State University, St. Petersburg 199034, Russia

(Received 21 February 2019; revised manuscript received 19 May 2019; published online 25 June 2019)

We discuss and illustrate the appearance of topological fermions and bosons in triple-point metals where a band crossing of three electronic bands occurs close to the Fermi level. Topological bosons appear in the phonon spectrum of certain triple-point metals, depending on the mass of atoms that form the binary triple-point metal. We first provide a classification of possible triple-point electronic topological phases possible in crystalline compounds and discuss the consequences of these topological phases, seen in Fermi arcs, topological Lifshitz transitions, and transport anomalies. Then we show how the topological phase of phonon modes can be extracted and proven for relevant compounds. Finally, we show how the interplay of electronic and phononic topologies in triple-point metals puts these metallic materials into the list of the most efficient metallic thermoelectrics known to date.

Keywords: topological metals, topological phonons, electronic structure, thermoelectrics

PACS: 73.20.At, 72.90.+y, 63.20.D–, 72.15.Jf **DOI:** 10.1088/1674-1056/28/7/077303

1. Introduction

Materials with non-trivial band structure topology, apart from possible technological applications, provide a test ground for the concepts of fundamental physics theories in relatively cheap condensed matter experiments. For example, the recent discovery of Weyl semimetals in TaAs materials class[1–5] provided materials in which two bands cross linearly at isolated points in momentum space as illustrated in Fig. 1(a), called Weyl points (WPs).[6] These WPs occur close to the Fermi level, and hence the low energy excitations in these metals are described by the Weyl equation of the relativistic quantum field theory, thus allowing for experimental studies of Weyl fermions, examples of which in high-energy physics are still lacking.

Another example of a topological material hosting a quasiparticle analogue of an elementary particle is that of Dirac semimetals.[7–10] These are centrosymmetric non-magnetic materials that host Dirac points (DPs) — points of linear crossing of two doubly degenerate bands in momentum space, see Fig. 1(b). When DPs are located close to the Fermi level, the low energy excitations of the hosting metal are described by the Dirac equation, and thus become direct analogues of Dirac electrons in high-energy theories.

More recently, it was shown that a variety of possible symmetries realized in solids also allow for the existence of topological quasiparticle excitations, which do not have direct analogues in the standard model,[11–19] rendering novel physical behavior to the hosting compounds. Classification and description of possible topologically protected quasiparticles in solids, along with the identification of material candidates, become of major importance for the progress in materials science and technology, as well as condensed matter theory in general.

The subject of this review is the so-called triple-point (TP) fermionic quasiparticle, which appears at the crossing of a singly and a doubly degenerate band, see Fig. 1(c).[20–23] Apart from the TPs, another class of topologically distinct threefold degenerate band crossing exists representing a spin-1 generalization of a Weyl fermion, see Fig. 1(d). While the TPs occur as accidental degeneracies in both symmorphic and non-symmorphic crystal structures, the latter is limited to high symmetry points in certain non-symmorphic space groups, containing symmetries combined of a point group symmetry operation followed by translation by a fraction of the primitive unit cell vector.[17] While the TPs described here can be also found in non-symmorphic space groups, the symmetry conditions for their appearance coincide in such cases with those of symmorphic space groups. The spin-1 fermion is furthermore characterized by a nontrivial Chern number, which is ill defined for the TPs due to the doubly degenerate band. The nontrivial topology of TPs, on the other hand, is manifested by topologically protected nodal lines and a $\mathbb{Z}_2$ topological classification applicable for pairs of TPs.

*G. W. W. and A. A. S. were supported by Microsoft Research and the Swiss National Science Foundation (SNSF) through the National Competence Centers in Research MARVEL and QSIT. A. A. S. acknowledges the support of the SNSF Professorship grant. S.S. acknowledges the support from the Dr. Mohindar S. Seehra Research Award.

†Corresponding author. E-mail: asoluyan@physik.uzh.ch

© 2019 Chinese Physical Society and IOP Publishing Ltd

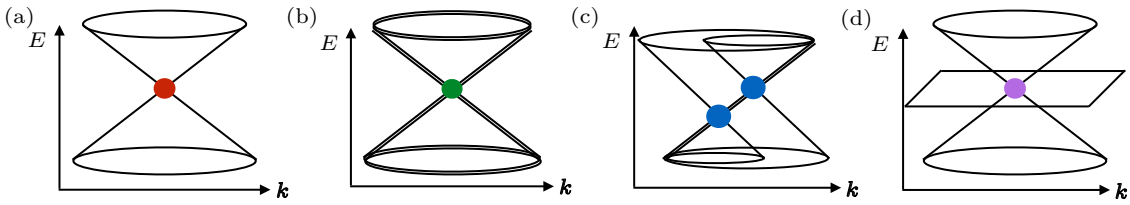


Fig. 1. (a) Weyl points are twofold degenerate band crossings of two singly degenerate bands. (b) Dirac points are fourfold degenerate band crossings of two twofold degenerate bands. (c) Triple-points are threefold degenerate band crossings of a singly and a doubly degenerate band. Here a pair is shown. (d) A spin-1 generalization of a Weyl fermion.[17]

2. Classification of triple-points

The realization of a symmorphic TP at a momentum $\boldsymbol{k}$ in the Brillouin zone (BZ) of a crystal structure requires the little group of $\boldsymbol{k}$ to contain both one- and two-dimensional double group representations, since both singly and doubly degenerate bands need to be present for the formation of the TP. Only the point group C_{3v} satisfies these criteria, thus TPs appear on high-symmetry lines in the BZ with the little group C_{3v}. The elements of C_{3v} are 3-fold rotation C_3 and 3 mirrors σ_v, containing the C_3 axis, rotated by 120° relative to each other.[24–26] One notable exception from this rule is given by space group 174 (C_{3h}^1), where the interplay of time-reversal and mirror symmetry on a C_3-symmetric line also allows for both one- and two-dimensional double group representations.

By using the above symmetry criterion, all space groups that can host TP fermions on a line are identified in Table 1. Note that the little group on the high-symmetry axis of the type-B TP topological metals (TPTMs) is exactly C_{3v}, while for type-A TPTMs it is supplemented by an additional anti-unitary symmetry. This symmetry is the product of a mirror plane σ_h orthogonal to the C_3-axis and time-reversal (TR). Its presence preserves the existence of doubly- and singly-degenerate representations, and hence, allows for the existence of TPs. In our consideration, we also included non-symmorphic space groups, such that the TP crossing includes the same irreducible representations as found in the symmorphic space groups.

The topological classification of TPs into type-A and type-B stems from the different numbers of accompanying nodal lines, and also from the fact that the nodal lines accompanying the two types of TPs are topologically distinct. Due to the three vertical mirror planes, the Berry phase φ_B accumulated by valence bands on any mirror-symmetric path (shown in grey in Figs. 2(c) and 2(d)) enclosing the corresponding nodal line is quantized to be either 0 or π.[27,28] The nodal line of type-A TPTMs has $\varphi_B = 0$, while all the lines of type-B TPs have $\varphi_B = \pi$.

Table 1. Space groups allowing for TPs of different types with time-reversal symmetry. The points can appear on high-symmetry lines in the Brillouin zone: $\Delta = (0,0,\alpha)$, $\Lambda = (\alpha,\alpha,\alpha)$, $P = (-1/3, 2/3, \alpha)$ (hexagonal lattice), $P = (1/2-\alpha, 1/2-\alpha, -1/2-\alpha)$ (rhombohedral lattice), and $F = (1/4+\alpha, 1/4-3\alpha, 1/4+\alpha)$. Triple-points appear in trigonal, hexagonal, and cubic space groups. Note that the table also contains non-symmorphic space groups but the TPs exist on lines where the non-symmorphicity does not change the irreducible representations, thus they are identical to the TPs found in the symmorphic space groups. The case of the non-symmorphic space group 220 has also been treated in Ref. [17]. We note that, in addition, the groups 162–167, 191–194, and 221–230 admit type-B TPs provided that time-reversal symmetry is broken in a way preserving C_{3v} representations on a line in the Brillouin zone.

TP type	Γ–A (Δ) or Γ–P_2 (Λ)	K–H (P) or P_0–T (P)	Γ–$L/R/P$ (Λ) or P–H (F)
Type-A	174, 187–190		
Type-B	156–161	157, 159–161, 183–186, 189–190	215–220

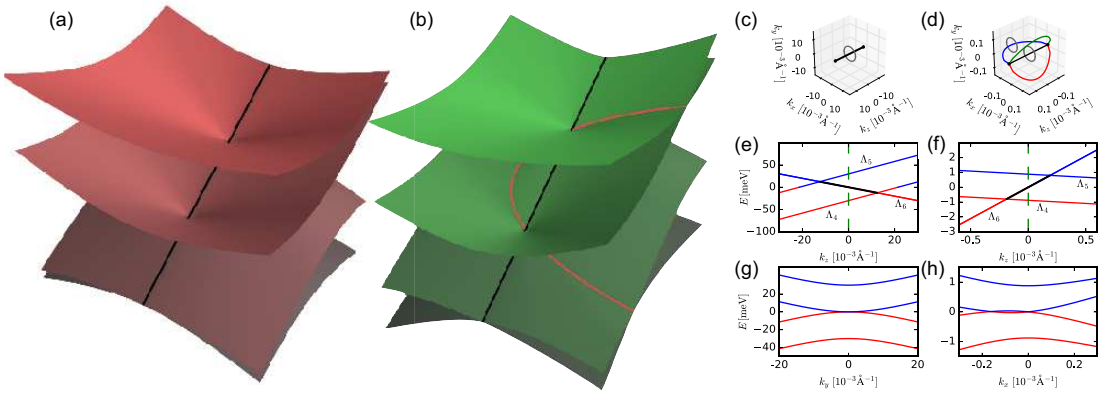


Fig. 2. Two types of fermionic triple-point quasiparticles. (a) and (c) Type-A triple-points are connected by a single nodal line, where conduction and valence bands are degenerate (shown in black). (b) and (d) Type-B triple-points are accompanied by four such nodal lines, shown in black, green, blue, and red. The latter three occur in the mirror-symmetric planes in momentum space. The grey circles in (c) and (d) indicate paths for the Berry phase calculation. (e) and (f) Band structures around type-A and type-B triple-points along the C_3 axis, respectively. Here Λ_6 represents the double degenerate band (double representation of C_{3v}), while $\Lambda_{4,5}$ correspond to two one-dimensional representations. The black lines in (e) and (f) mark the region of the band structure that produces the nodal lines shown in black in panels (c) and (d). (g) and (h) Band structures around type-A and type-B triple-points in a mirror symmetric plane orthogonal to k_z, respectively. The dashed green lines in (e) and (f) mark the momentum k_z used in panels (g) and (h). Red (blue) color in panels (e)–(h) corresponds to occupied (unoccupied) bands assuming that the Fermi level is exactly between the pair of triple-points. Figure partially reused from Ref. [21].

These values are consistent with the band structure plots shown in Figs. 2(e)–2(h). In type-A TPTMs, the crossing of conduction and valence (occupied and unoccupied) bands occurs on a high-symmetry line and is quadratic, while for the type-B phase this quadratic touching point splits into two points, where the bands cross linearly. The presence of nodal lines with nontrivial Berry phase, as is the case for type-B, is generally associated with the appearance of surface states.[28,29] The merging and subsequent annihilation of nodal lines are similar to those of the nexus point discussed in the context of ^{3}He-A and Bernal-stacked graphite with neglected spin–orbit coupling (SOC).[30–33] We stress, however, that the scenarios discussed in the present work take full account of SOC.

Analogous to WPs,[6] the minimal number of TPs in the BZ is four for materials preserving time-reversal symmetry. A pair of TPs located on a C_{3v}-symmetric line can be split into four WPs by lowering the C_{3v} symmetry to C_3 (breaking σ_v), which can be achieved by a small Zeeman field parallel to the C_3 axis or by an atomic distortion. Conversely, imposing inversion symmetry onto the atomic structure makes the two TPs merge into a single DP. Hence, the TPTMs can be viewed as an intermediate phase separating Dirac and Weyl semimetals in materials with a C_{3v}-symmetric line in the BZ.

3. Triple-point materials

The possibility of new fermions in condensed matter systems sparked a huge effort in the first-principles community to look for suitable material candidates. While band structures with threefold degenerate crossings appear to be comparatively rare in nature, using extensive scans of material databases enabled by high-throughput calculations, a decent amount of material candidates for TPTMs could still be identified. Experimental investigations of some of these materials are currently under way with some results already published.[34–38] In Table 2, we list all TPTMs that have been predicted by first-principles methods up to the point of this writing.

Table 2. Theoretically predicted TPTMs classified in type-A and type-B. Material candidates for which experimental evidence of TPs exists are marked by an asterisk.

TP type	Material
Type-A	MoC,[21,39] WC*,[21,34,35] WN,[21] ZrTe,[21,40] MoP*,[21,36,37] MoN,[21] TaN,[21,22] NbN,[21] NbS,[21] TaS,[41] TaSb[42]
Type-B	tensile strained HgTe[43], CuPt-ordered InAsSb*,[20,38] CuAgSe,[44] LuPtBi,[45] LuAuPb,[45] YPtBi,[45] GdPtBi,[45] LuPtBi,[45] LaPtBi[45]

The TPTMs have been predicted in three types of crystal structures: type-A TPTMs are exclusively of a tungsten carbide (WC) structure and type-B TPTMs either have cubic symmetry (HgTe, half-Heuslers) or are obtained by breaking the cubic T_d symmetry to the subgroup C_{3v} (tensile strained HgTe, CuPt-ordered InAsSb).

3.1. Triple-points in tungsten carbide like crystal structure

The type-A TPTM phase has been identified in a family of two-element metals AB ($A = \{$Zr, Nb, Mo, Ta, W$\}$, $B = \{$C, N, P, S, Te, Sb$\}$) listed in the type-A row of Table 2. These materials have a WC-type structure that belongs to space group $P\bar{6}m2$ ($D^1_{3h} = 187$). The primitive unit cell, shown in Fig. 3(a), consists of two atoms A and B at Wyckoff positions $1a$ $(0,0,0)$ and $1d$ $(1/3,2/3,1/2)$, respectively. The corresponding bulk BZ is shown in Fig. 3(b) along with the (001) and (010) surface BZs.

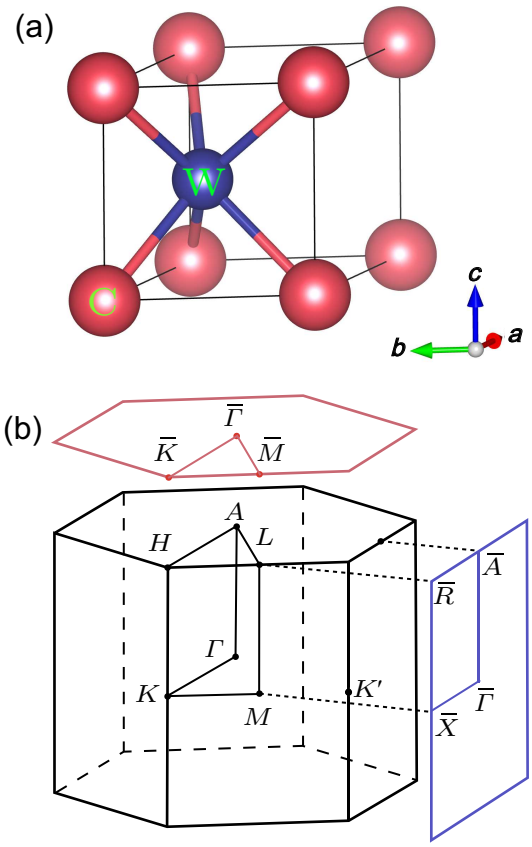


Fig. 3. (a) Primitive unit cell of WC-type structure. (b) The bulk BZ and (001) and (010) surface BZs. Figure reused from Ref. [21].

Now we discuss the band structure obtained by *ab initio* simulations.[21] Figure 4 shows the band structures of ZrTe, WC, and TaN, which will be used as representative materials.

In the absence of SOC, there is a band inversion at K and K' points in ZrTe and WC (Figs. 4(a) and 4(c)), resulting in a nodal ring in the $k_z = 0$ plane protected by σ_h, while this band inversion is absent in TaN. The common feature of all materials is that along the C_{3v}-symmetric Γ–A line, there is a band crossing of the singly and doubly degenerate bands due to the

inversion of the singly- (Λ_1) and the doubly-degenerate (Λ_3) states at A. This crossing produces a single no-SOC TP, and it is this feature that generates four TPs upon introducing SOC.

All the considered materials have sizable SOC, which cannot be neglected. Due to the lack of inversion symmetry, the bands are spin-split at generic momenta as shown in Figs. 4(b), 4(d), and 4(f). One finds a band inversion along the H–A–L line such that the A point acquires an inverted gap for all materials. Consequently, the $k_z = \pi$ plane becomes an analogue of a 2D quantum spin Hall insulator in all of the compounds. Topological confirmation of the presence of band inversion is given by the non-trivial values of the mirror Chern numbers[46] on the σ_h planes, see Fig. 5, which are $C_{\pm i} = \mp 1$, for the mirror eigenvalues $\pm i$, respectively in the $k_z = \pi$ plane for the materials considered here.[21] In the $k_z = 0$ plane, one finds $C_{\pm i} = \mp 1$ for ZrTe, MoP, and NbS and $C_{\pm i} = 0$ for MoN, TaN, and NbN. The materials MoC, WC, and WN have nodal lines in the $k_z = 0$ plane and, therefore, the mirror Chern number is ill defined for them.

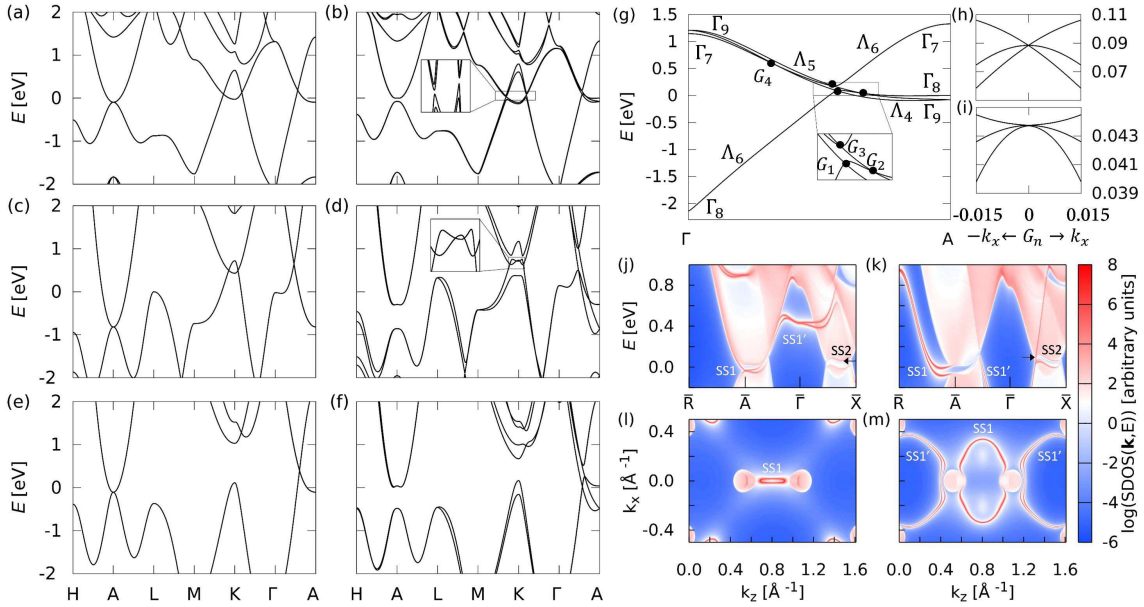


Fig. 4. Band structures of (a) ZrTe, (c) WC, and (e) TaN without SOC. Those with SOC are correspondingly shown in panels (b), (d), and (f). The Fermi energy is set to 0 eV. (g) Band structure of ZrTe along the Γ–A line. Bands are labeled by their double group representations corresponding to D_{3h} at Γ and A points and C_{3v} on the Γ–A line. (h) and (i) Band structures in the (100) direction with k_z tuned to the TPs G_1 and G_2, respectively. (j) and (k) Projected surface density of states (SDOS) for the (010) surface of ZrTe with (j) Zr and (k) Te termination. (l) and (m) The (010)-surface Fermi surface of ZrTe at $E = 0$ eV for (l) Zr and (m) Te termination. Figure reused from Ref. [21].

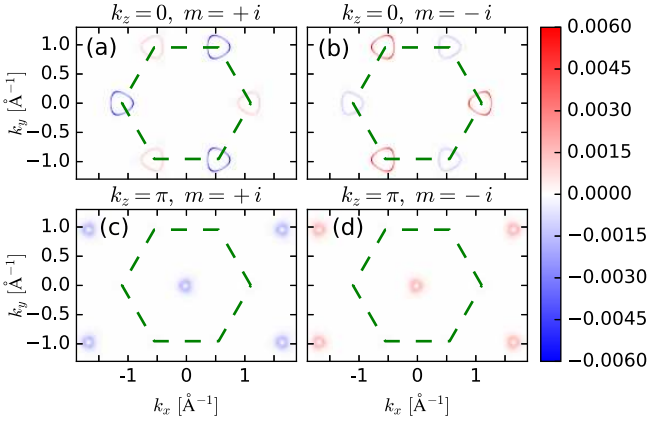


Fig. 5. The Berry curvature for (a)–(d) specific mirror eigenvalues on σ_h-mirror invariant planes in ZrTe. Figure reused from Ref. [21].

In ZrTe, the nodal ring around K and K' points acquires a small gap (see also the inset in Fig. 4(b)). Interestingly, three pairs of WPs, slightly away from the $k_z = 0$ plane, form at each K and K' point in ZrTe[40] and also in MoP.[36] WC (together with MoC and WN) remains a nodal line metal (see inset of Fig. 4(d)). There exist two nodal rings (one inside another) formed by two touching bands protected by the horizontal mirror σ_h. For WN, there is only a single such nodal ring around each K and K'. The stability of these topological features has been checked with the HSE06 hybrid functional.[21,47] Furthermore, the band structure of MoP has been recently experimentally investigated using angle-resolved photoemission spectroscopy (ARPES), confirming experimentally the presence of TPs and WPs.[36]

In Fig. 4(g), a zoom-in of the Γ–A line in ZrTe is shown. The Fermi level resides in between the Γ_9 and Γ_8 bands at A. Upon turning on the SOC, the no-SOC Λ_3 state splits into the singly degenerate $\Lambda_4 + \Lambda_5$ states and the doubly degenerate Λ_6 state. Another Λ_6 state comes from the no-SOC Λ_1. The two Λ_6 states hybridize and each of them crosses with the spin-split $\Lambda_{4,5}$ states, creating 2 pairs of TPs: (G_1, G_2) and (G_3, G_4). Each TP is protected by the C_{3v} symmetry of the Γ–A line. Figures 4(h) and 4(i) show the dispersions in the (100) direction for k_z tuned to the positions G_1 and G_2, respectively. A linear band crossing superimposed with a quadratic band re-

sembles a WP, degenerate with a quadratic band, similar to the findings of Ref. [20] for type-B TPTMs. Again, band inversion is the mechanism leading to the formation of TPs.

In Figs. 4(j) and 4(k), the surface states of ZrTe for the (010) surface are shown.[21,48] The surface potential is found to depend strongly on the termination choice: Zr (Te)-termination is shown in Fig. 4(j) (Fig. 4(k)). Since the $k_z = \pi$ plane is a quantum spin Hall insulator plane, a Kramers doublet of surface states should appear along the $\overline{A}$–$\overline{R}$ line of the surface BZ. Consequently, there is a surface Dirac cone SS1 located at $\overline{A}$ ($\overline{R}$) for Zr (Te) termination. The surface states forming the Dirac cone emerge from the TPs G_1 and G_2. For k_z values below the location of G_1 and G_2, there exists another pair of surface states SS1′ emerging from the TPs. SS1′, however, is not topologically protected.

The K' point of the bulk BZ is projected onto the $\overline{\Gamma}$–$\overline{X}$ line in Figs. 4(j) and 4(k) (compare to Fig. 3(b)). A small gap due to SOC can be visible in the projected bulk spectrum around the projection of K point (shown with an arrow). For ZrTe, the $k_z = 0$ mirror plane hosts a quantum spin Hall phase with the mirror Chern numbers ± 1, thus one can expect to see a Kramers pair of topological surface states along the line $\overline{X} \leftarrow \overline{\Gamma} \rightarrow -\overline{X}$. This expectation is further supported by the Berry curvature calculation in the $k_z = 0$ plane, see Fig. 5. It reveals the accumulation of Berry curvature in an area around the K (K') point that sums up to approximately -1 (1).[21] In accord with this topological arguments, one finds a quantum Hall like surface state SS2 crossing the gap along $\overline{\Gamma}$–$\overline{X}$ (its Kramers partner is not shown, being at TR-symmetric part of the surface BZ.

Figures 4(l) and 4(m) show the (010)-surface Fermi surface revealing double Fermi arcs between the two hole pockets containing the TPs, corresponding to SS1 and SS1′. The state SS2 is not visible for this choice of the Fermi level. For the Te termination, the Fermi arcs connect the two hole pockets, while they do not touch the hole pockets for the Zr termination. In both cases, however, the surface states are protected by TR and mirror symmetry on the $k_z = \pi$ plane, so they cannot be fully removed from the spectrum. ARPES investigations of the very similar TPTM WC prove the existence of the surface Fermi arcs SS1 and SS1′.[35]

3.2. Cubic symmetry

One of the first account of TPs has been given in the context of HgTe by Saad Zaheer *et al.* in Ref. [43]. According to the cubic symmetry, there are eight equivalent directions with little group C_{3v} hosting possible TPs. Due to the lack of a horizontal mirror, these TPs are all of type-B. The situation is complicated by the fact that the $\Lambda_{4,5}$ and Λ_6 states are degenerate at Γ forming the four-dimensional Γ_8 representation. This leads generically to eight TPs near a Γ_8 crossing along the eight equivalent Λ directions, see Fig. 6(a). However, in the HgTe case, the TPs are extremely close to Γ such that they are impossible to resolve with available experimental techniques.

The same scenario takes place in half-Heusler compounds with band inversion.[49] Interestingly, in some compounds like LuPtBi, LuAuPb, and YPtBi, the energy bands have such a strong non-parabolicity that additional TPs appear.[45] The evolution of the band structure with increasing number of TPs is illustrated in Figs. 6(b) and 6(d). Therefore these half-Heusler compounds have three TPs in each equivalent 111 direction, 24 in total. Furthermore, these TPs are well separated from the Γ point with observable Fermi arcs on the easily cleavable (111) surface.[45,50,51] These properties make the half-Heusler compounds ideally suited to experimentally investigate the intricate topology and surface states of type-B TPs.

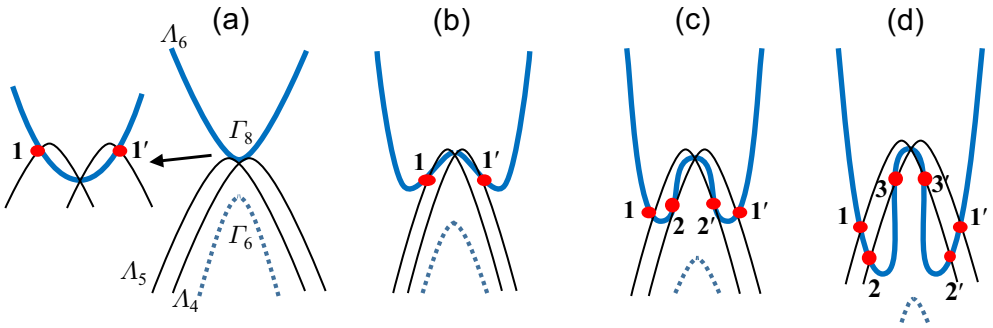


Fig. 6. Energy bands along L–Γ–L in cubic crystals with band inversion. The thick blue line is doubly degenerate whereas black lines are non-degenerate. (a) HgTe-type energy bands. (b)–(d) Evolution of band structure in half-Heusler materials with increasing number of TPs. Illustration adapted with permission from Ref. [45].

3.3. CuPt-ordered $InAs_{1-x}Sb_x$

Above we have seen that the TPs of the cubic HgTe are too close to Γ to enable a direct experimental observation. However, this can be changed by applying a moderate tensile strain in the 111 direction, such that the remaining point group is broken down from T_d to C_{3v}.[43] In this case, two pairs of TPs survive. Unfortunately, it is experimentally difficult to apply 111 strain to HgTe. The ingredients to achieve well separated TPs in HgTe are band inversion and breaking of cubic T_d symmetry to C_{3v}. It is no surprise that the

same ideas can be applied in other III–V semiconductors. The difficulty of applying 111 strain can be overcome by changing the mechanism of symmetry breaking from strain to alloy ordering. Fortunately, some ternary III–V compounds show naturally a so-called CuPt-ordering,[52] which is ordering in alternating 111 planes, see Fig. 7(a). This type of ordering provides exactly the desired symmetry breaking. Especially promising is the $InAs_{1-x}Sb_x$ system.[20] InAs and InSb are both small band gap semiconductors and the band gap is further reduced in their alloy.[53–55] CuPt-ordering further reduces the band gap[52,56,57] and first-principles calculations show that the perfectly CuPt-ordered $InAs_{0.5}Sb_{0.5}$ alloy has an inverted band order.[20,58] While perfect atomic CuPt-ordering in $InAs_{0.5}Sb_{0.5}$ is difficult to obtain, the same effect is achieved by growing layered structures of $InAs_{1-x}Sb_x$ with alternating alloy composition x. With this approach, the band gap can be tuned from normal to inverted band ordering.[38,59]

The band structure of CuPt-ordered $InAs_{0.5}Sb_{0.5}$ obtained from first-principles simulations is shown in Fig. 7(b).[20] A pair of TPs is formed at the crossings of the $\Lambda_{4,5}$ with the Λ_6 band. The $\Lambda_{4,5}$ bands have a very small linear in k, splitting, which is only about 2 meV at the momentum of the TPs. The pair of TPs is thus very close together and will appear like a single Dirac point in low resolution experiments.

Another very interesting aspect of CuPt-ordered $InAs_{1-x}Sb_x$ is that the symmetry breaking to C_{3v} simultaneously allows for a Rashba-type spin–orbit splitting in the conduction band, provided that the band order is normal. Either by imperfect CuPt-ordering, or by 111 strain, the normal band order can be restored and one obtains a giant-Rashba material, see Fig. 7(c). Large Rashba splitting is a crucial ingredient for topological quantum computers relying on non-abelian Majorana,[60–64] quasiparticles realized in semiconductor nanowires.[65,66] Since InAs and InSb are the preferred materials for the experimental realizations of Majorana quasiparticles,[67–71] CuPt-ordered $InAs_{1-x}Sb_x$ seems to be a very promising material for this application.[20]

Figures 7(e) and 7(f) show the surface density of states of the $(1\bar{1}0)$ surface.[20] In this case, the Fermi arcs resulting from the TPs look very similar to those from the typical Dirac semimetals[7,8,10] due to the small separation of the TPs.

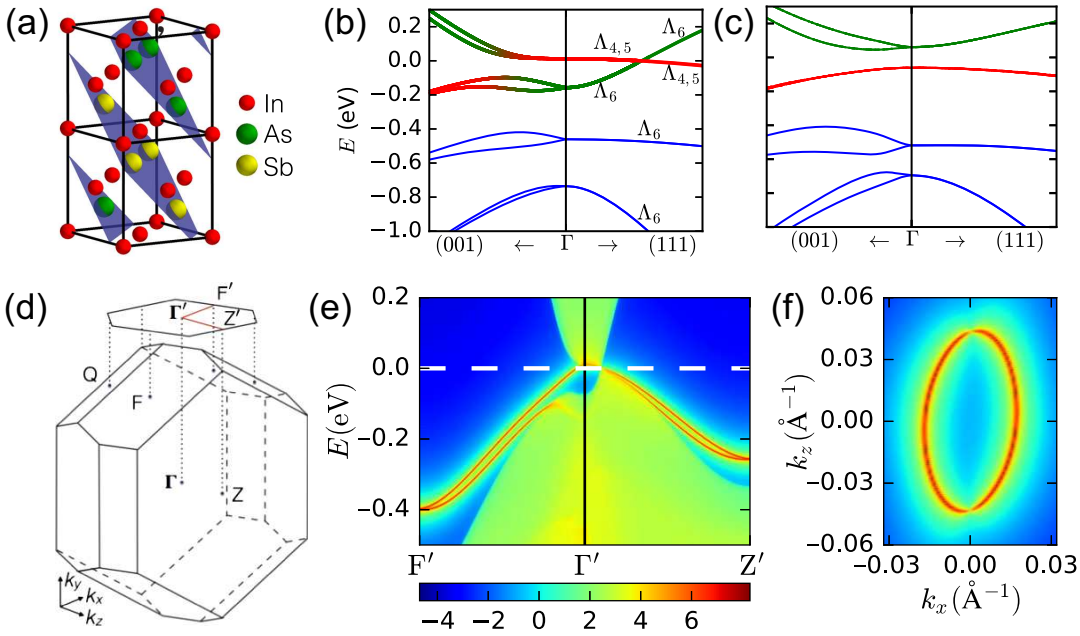


Fig. 7. (a) Crystal structure of CuPt-ordered $InAs_{0.5}Sb_{0.5}$. (b) Band structure of CuPt-ordered $InAs_{0.5}Sb_{0.5}$ around Γ (plotted up to $|\boldsymbol{k}| = 0.1$ Å^{-1}). (c) Band structure with 3% compressive strain applied in the 111-direction. (d) Brillouin zone and surface projection of CuPt-ordered $InAs_{0.5}Sb_{0.5}$. (e) Surface density of states for the $(1\bar{1}0)$ surface. (f) Topological Fermi arcs on the $(1\bar{1}0)$ surface. Figure partially reused from Ref. [20].

4. Topological properties of the triple-point fermions

In this section, we first introduce simplified models of TP materials and use them to discuss the topological properties of TPs.

4.1. Microscopic models

Before we investigate the topology of TPs, we introduce a few simple $\boldsymbol{k}\cdot\boldsymbol{p}$-models for type-A and type-B triple-points. The type-A $\boldsymbol{k}\cdot\boldsymbol{p}$-models are up to a change of basis identical to the ones in Ref. [21] and the given parameters correspond to the material realization of ZrTe. The type-B $\boldsymbol{k}\cdot\boldsymbol{p}$-models are also up to a basis transformation identical to the ones in Ref. [20] and the parameters correspond to the CuPt-ordered $InAs_{0.5}Sb_{0.5}$ case.

4.1.1. Type-A: ZrTe

For the WC-class of type-A TPTMs, we construct a model around the A point which captures the band inversion

and describes the TPs. We include the Γ_9, Γ_8, and Γ_7 states (see Fig. 4(g) and Table 65 of Ref. [24]) with energies close to the Fermi level. Along the z-axis, the Γ_9 representation splits into the $\Lambda_{4,5}$ representations and both $\Gamma_{7,8}$ become Λ_6. The little group of A is D_{3h} plus TR symmetry. For the derivation of the $\boldsymbol{k}\cdot\boldsymbol{p}$ models, we need to identify the correct representations of the symmetry operations. The Hamiltonian is then constructed such that it commutes with all symmetries S

$$H(S(\boldsymbol{k})) = R_S H(\boldsymbol{k}) R_S^{\dagger}, \tag{1}$$

with R_S being the representation of S in the basis of H. Since all representations are two dimensional, the symmetry representation is the direct sum of two-dimensional representations

$$R(\Gamma_9)\oplus R(\Gamma_7)\oplus R(\Gamma_8),$$

$$\begin{aligned}
C_3 &= \begin{pmatrix} -\frac{1}{2} & -\frac{\sqrt{3}}{2} & \\ \frac{\sqrt{3}}{2} & -\frac{1}{2} & \\ & & 1 \end{pmatrix},\\
R_{C_3} &= \mathrm{diag}\left(-1,-1,\mathrm{e}^{-\mathrm{i}\pi/3},\mathrm{e}^{\mathrm{i}\pi/3},\mathrm{e}^{-\mathrm{i}\pi/3},\mathrm{e}^{\mathrm{i}\pi/3}\right),\\
\sigma_v &= \mathrm{diag}(-1,1,1), \qquad R_{\sigma_v} = \mathrm{i}\,\mathrm{diag}(1,1,1)\otimes\tau_x,\\
\sigma_h &= \mathrm{diag}(1,1,-1), \qquad R_{\sigma_h} = \mathrm{i}\,\mathrm{diag}(1,1,-1)\otimes\tau_z,\\
\mathrm{TR} &= \mathrm{diag}(-1,-1,-1), \quad R_{\mathrm{TR}} = -\mathrm{i}\,\mathrm{diag}(1,1,1)\otimes\tau_y,
\end{aligned} \tag{2}$$

with τ_x, τ_y, and τ_z being the Pauli matrices.

Considering the constraint Eq. (1) for all symmetries above, one obtains the following Hamiltonian:

$$H^{\mathrm{A}}_{\boldsymbol{k}\cdot\boldsymbol{p}} = \begin{pmatrix}
\varepsilon_1 & Ak_z & E(k_x-y) & 0 & 0 & D(-\mathrm{i}k_x+k_y)\\
Ak_z & \varepsilon_1 & 0 & E(-k_x-\mathrm{i}k_y) & D(\mathrm{i}k_x+k_y) & 0\\
E(k_x+\mathrm{i}k_y) & 0 & \varepsilon_2 & 0 & -\mathrm{i}Bk_z & C(-\mathrm{i}k_x-k_y)\\
0 & E(-k_x+\mathrm{i}k_y) & 0 & \varepsilon_2 & C(\mathrm{i}k_x-k_y) & -\mathrm{i}Bk_z\\
0 & D(-\mathrm{i}k_x+k_y) & \mathrm{i}Bk_z & C(-\mathrm{i}k_x-k_y) & \varepsilon_3 & 0\\
D(\mathrm{i}k_x+k_y) & 0 & C(\mathrm{i}k_x-k_y) & \mathrm{i}Bk_z & 0 & \varepsilon_3
\end{pmatrix}, \tag{3}$$

using the definition $\varepsilon_i(\boldsymbol{k}) = E_i + F_i(k_x^2+k_y^2) + G_i k_z^2$ and $\boldsymbol{k}$ relative to the A point. Via fitting to the ZrTe band structure, we obtain the following parameters for Eq. (3): $E_1 = -0.0391$ eV, $E_2 = 1.3709$ eV, $E_3 = 0.0391$ eV, $F_1 = 3.75$ eV·Å^2, $F_2 = -0.5$ eV·Å^2, $F_3 = 4.25$ eV·Å^2, $G_1 = 2.2$ eV·Å^2, $G_2 = -12.64$ eV·Å^2, $G_3 = 1.5$ eV·Å^2, $A = 0.17$ eV·Å, $B = 0.24$ eV·Å, $C = 2.9$ eV·Å, $D = 0.054$ eV·Å, and $E = 2.76$ eV·Å.

If the influence of the Γ_7 state is removed, one obtains a 4×4 model

$$H^{\mathrm{A},4\times4}_{\boldsymbol{k}\cdot\boldsymbol{p}} = \begin{pmatrix}
\varepsilon_1 & Ak_z & 0 & D(-\mathrm{i}k_x+k_y)\\
Ak_z & \varepsilon_1 & D(\mathrm{i}k_x+k_y) & 0\\
0 & D(-\mathrm{i}k_x+k_y) & \varepsilon_3 & 0\\
D(\mathrm{i}k_x+k_y) & 0 & 0 & \varepsilon_3
\end{pmatrix}. \tag{4}$$

To simulate the interaction of the two Λ_6 bands, we add a fourth order term to $\varepsilon_3(\boldsymbol{k}) = E_3 + F_3(k_x^2+k_y^2) + G_3 k_z^2 + H_3 k_z^4$. We find the following parameters via fitting to the band structure of ZrTe: $E_1 = -0.0391$ eV, $E_3 = 0.0391$ eV, $F_1 = 4.5$ eV·Å^2, $F_3 = -7.3$ eV·Å^2, $G_1 = 2.2$ eV·Å^2, $G_3 = 3.2$ eV·Å^2, $H_1 = 0$ eV·Å^4, $H_3 = -20$ eV·Å^4, $A = 0.17$ eV·Å, and $D = 0.487$ eV·Å. Note that the parameter A is the only one that breaks inversion symmetry in the above model. Setting $A = 0$, one obtains a $\boldsymbol{k}\cdot\boldsymbol{p}$ description of a Dirac semimetal.

A four-band Hamiltonian in the vicinity of a pair of TPs, where $\boldsymbol{k}$ is understood relative to the midpoint of the two TPs, is given below

$$H^{\mathrm{TP_A}}_{\boldsymbol{k}\cdot\boldsymbol{p}} = \begin{pmatrix}
A_1k_z & A_2k_z+E_0 & \mathrm{i}D(k_x-\mathrm{i}k_y) & \mathrm{i}C(k_x+\mathrm{i}k_y)\\
A_2k_z+E_0 & A_1k_z & \mathrm{i}C(k_x-\mathrm{i}k_y) & \mathrm{i}D(-k_x-\mathrm{i}k_y)\\
-\mathrm{i}D(k_x+\mathrm{i}k_y) & -\mathrm{i}C(k_x+\mathrm{i}k_y) & Bk_z & 0\\
-\mathrm{i}C(k_x-\mathrm{i}k_y) & -\mathrm{i}D(-k_x+\mathrm{i}k_y) & 0 & Bk_z
\end{pmatrix}. \tag{5}$$

Instead of σ_h and TR, only their product $\theta\circ\sigma_h$ needs to be taken into account at a general $\boldsymbol{k}$-point on the C_{3v}-symmetric z-axis. In the following, we use $E_0 = 30$ meV, $A_1 = 1.4$ eV·Å, $A_2 = 0$ eV·Å, $B = -1.0$ eV·Å, $C = 1.082$ eV·Å, and $D = 0$ eV·Å. We use the above $\boldsymbol{k}\cdot\boldsymbol{p}$ model for the illustrations of the type-A TPTM in Fig. 2.

The WC-class of TPTMs also has interesting topological properties around the K-points. A good $\boldsymbol{k}\cdot\boldsymbol{p}$ description of the topology and bands around K (or K') requires at least 8 states. The little group of the K points is C_{3h} and the Γ_7, Γ_{12}, Γ_{11}, Γ_9, Γ_{12}, Γ_{10}, Γ_8, and Γ_7 states (see Table 57 of Ref. [24]) are determined to be relevant for constructing a $\boldsymbol{k}\cdot\boldsymbol{p}$-description. We use the following symmetry representations:

$$\begin{aligned}
C_3 &= \begin{pmatrix} -\frac{1}{2} & -\frac{\sqrt{3}}{2} & \\ \frac{\sqrt{3}}{2} & -\frac{1}{2} & \\ & & 1 \end{pmatrix},\\
R_{C_3} &= \mathrm{diag}\left(\mathrm{e}^{\mathrm{i}\frac{\pi}{3}},-1,-1,\mathrm{e}^{\mathrm{i}\frac{\pi}{3}},-1,\mathrm{e}^{-\mathrm{i}\frac{\pi}{3}},\mathrm{e}^{-\mathrm{i}\frac{\pi}{3}},\mathrm{e}^{\mathrm{i}\frac{\pi}{3}}\right),\\
\sigma_h &= \mathrm{diag}\{1,1,-1\}, \quad R_{\sigma_h} = \mathrm{diag}(\mathrm{i},-\mathrm{i},\mathrm{i},-\mathrm{i},-\mathrm{i},\mathrm{i},-\mathrm{i},\mathrm{i}).
\end{aligned} \tag{6}$$

Considering the symmetries given above, the lowest order Hamiltonian around K is given by

$$H^{K}_{\boldsymbol{k}\cdot\boldsymbol{p}} = \begin{pmatrix}
\varepsilon_1 & 0 & B_1k^+ & A_1k_z & 0 & B_3k^- & 0 & 0\\
0 & \varepsilon_2 & -A_1'k_z & B_2k^- & 0 & 0 & B_4k^+ & 0\\
B_1^*k^- & -A_1'^*k_z & \varepsilon_3 & 0 & A_2k_z & B_9k^+ & 0 & B_5k^-\\
A_1^*k_z & B_2^*k^+ & 0 & \varepsilon_4 & -B_9'k^+ & 0 & B_6k^- & A_4k_z\\
0 & 0 & A_2^*k_z & -B_9'^*k^- & \varepsilon_5 & 0 & B_7k^+ & 0\\
B_3^*k^+ & 0 & B_9^*k^+ & 0 & 0 & \varepsilon_6 & A_3k_z & B_8k^+\\
0 & B_4^*k^- & 0 & B_6^*k^+ & B_7^*k^- & A_3^*k_z & \varepsilon_7 & 0\\
0 & 0 & B_5^*k^+ & A_4^*k_z & 0 & B_8^*k^- & 0 & \varepsilon_8
\end{pmatrix}, \tag{7}$$

using ε_i defined in Eq. (3), $k^{\pm} = k_x \pm \mathrm{i}k_y$, and $\boldsymbol{k}$ relative to K. Since K is not a time-reversal invariant momentum, bands

do not form doubly degenerate Kramers pairs at this point. For the $\boldsymbol{k}\cdot\boldsymbol{p}$ model around the K point, we obtain the following parameters (in units of eV and Å) via fitting to the ZrTe band structure: $E_1 = -0.0979$, $E_2 = -0.0671$, $E_3 = 0.6538$, $E_4 = 0.8393$, $E_5 = 1.0661$, $E_6 = 1.1351$, $E_7 = 1.2145$, $E_8 = 1.2774$, $F_1 = F_2 = 3.6$, $F_3 = F_4 = -2.0$, $F_5 = F_6 = 6.0$, $F_7 = F_8 = 1.5$, $G_1 = G_2 = 3.6$, $G_3 = G_4 = -0.2$, $G_5 = G_6 = 2.0$, $G_7 = G_8 = -3.0$, $A_1 = A_1' = 4.0$, $A_2 = 0.2$, $A_3 = 0$, $A_4 = 0$, $B_1 = 0.2 - \mathrm{i}0.1$, $B_2 = 0.02 - \mathrm{i}0.01$, $B_3 = 0.2$, $B_4 = -0.2$, $B_5 = -1.0 + \mathrm{i}4.0$, $B_6 = -4.0 + \mathrm{i}1.0$, $B_7 = 3.0 + \mathrm{i}0.5$, $B_8 = -0.5 + \mathrm{i}3.0$, and $B_9 = 1.5$. The Weyl points reported in Ref. [40] are also described by this $\boldsymbol{k}\cdot\boldsymbol{p}$ model.

4.1.2. Type-B: CuPt-ordered $InAs_{0.5}Sb_{0.5}$

The type-B scenario differs only by the absence of the horizontal mirror σ_h. For completenes, we give the corresponding representations again, albeit σ_v is now a mirror in the xz-plane instead of the xy-plane as before. The representations below correspond to a $\Lambda_{4,5}\oplus\Lambda_6$-basis

$$
\begin{aligned}
&C_3 = \begin{pmatrix} -\frac{1}{2} & -\frac{\sqrt{3}}{2} & \\ \frac{\sqrt{3}}{2} & -\frac{1}{2} & \\ & & 1 \end{pmatrix}, \quad R_{C_3} = \mathrm{diag}\left(-1,-1,\mathrm{e}^{-\mathrm{i}\pi/3},\mathrm{e}^{\mathrm{i}\pi/3}\right),\\
&\sigma_v = \mathrm{diag}(1,-1,1), \quad R_{\sigma_v} = \mathrm{i}\,\mathrm{diag}(1,1)\otimes\tau_y,\\
&\mathrm{TR} = \mathrm{diag}(-1,-1,-1), \quad R_{\mathrm{TR}} = -\mathrm{i}\,\mathrm{diag}(1,1,1)\otimes\tau_y. \qquad (8)
\end{aligned}
$$

Around Γ the following model is obtained:

$$
H^{\mathrm{B}}_{\boldsymbol{k}\cdot\boldsymbol{p}} = \begin{pmatrix} \varepsilon_1 & -\mathrm{i}Ak_z & \mathrm{i}B_1(k_x-\mathrm{i}k_y) & \mathrm{i}B_2(k_x+\mathrm{i}k_y) \\ \mathrm{i}Ak_z & \varepsilon_1 & \mathrm{i}B_2(k_x-\mathrm{i}k_y) & \mathrm{i}B_1(-k_x-\mathrm{i}k_y) \\ -\mathrm{i}B_1(k_x+\mathrm{i}k_y) & -\mathrm{i}B_2(k_x+\mathrm{i}k_y) & \varepsilon_2 & \mathrm{i}C(k_x-\mathrm{i}k_y) \\ -\mathrm{i}B_2(k_x-\mathrm{i}k_y) & -\mathrm{i}B_1(-k_x+\mathrm{i}k_y) & -\mathrm{i}C(k_x+\mathrm{i}k_y) & \varepsilon_2 \end{pmatrix}, \qquad (9)
$$

with the following set of parameters for CuPt-ordered $InAs_{0.5}Sb_{0.5}$: $E_1 = 0.1696$ eV, $E_2 = 0$ eV, $F_1 = -5.86$ eV·Å^2, $F_2 = 14.3$ eV·Å^2, $G_1 = -3.91$ eV·Å^2, $G_2 = 54.2$ eV·Å^2, $A = 0.02$ eV·Å, $B_1 = 0$,$B_2 = 1.48$ eV·Å, and $C = 1.26$ eV·Å.

Omitting the TR symmetry, a Hamiltonian of a pair of TPs, with $\boldsymbol{k}$ relative to the midpoint of the two TPs, is obtained as

$$
H^{\mathrm{TP_B}}_{\boldsymbol{k}\cdot\boldsymbol{p}} = \begin{pmatrix} A_1k_z & -\mathrm{i}(A_2k_z+E_0) & F(k_x-\mathrm{i}k_y) & D(k_x+\mathrm{i}k_y) \\ \mathrm{i}(A_2k_z+E_0) & A_1k_z & D(-k_x+\mathrm{i}k_y) & F(k_x+\mathrm{i}k_y) \\ F^*(k_x+\mathrm{i}k_y) & D^*(-k_x-\mathrm{i}k_y) & Bk_z & C(\mathrm{i}k_x+k_y) \\ D^*(k_x-\mathrm{i}k_y) & F^*(k_x-\mathrm{i}k_y) & C(-\mathrm{i}k_x+k_y) & Bk_z \end{pmatrix}. \qquad (10)
$$

In contrast to Eq. (5), the parameters D and F can now take complex values. We use $E_0 = 0.88$ meV, $A_1 = -0.42$ eV·Å, $A_2 = 0$ eV·Å, $B = 4.22$ eV·Å, $C = 0.78$ eV·Å, $D = 0.755 - 0.445\mathrm{i}$, and $F = -1.69 + 0.755\mathrm{i}$. We use the above $\boldsymbol{k}\cdot\boldsymbol{p}$ model for the illustrations of the type-B TPTM in Fig. 2.

4.2. Wilson loop characterization for pairs of triple-points

The tracking of Wilson loop eigenvalues,[72] or equivalently the so-called hybrid Wannier centers,[73] under an adiabatic modification of a Hamiltonian has been proven as an invaluable tool for classifying topological phases.[11,74–76] Here a $\mathbb{Z}_2$ topological classification based on the Wilson loop is developed for pairs of TPs.

The Wilson loop can be defined on any path in k-space connecting two points $\boldsymbol{k}_1$ and $\boldsymbol{k}_2$ with the property $\boldsymbol{k}_1 = \boldsymbol{k}_2 + \boldsymbol{G}$, where $\boldsymbol{G}$ is a reciprocal lattice vector. The Wilson loop is defined as the path ordered product[72]

$$
\mathscr{W}_{\boldsymbol{k}_1\boldsymbol{k}_2} = P_{\boldsymbol{k}_1}\left(\prod_{j=1,2,\ldots} P_{\boldsymbol{k}'_j}\right)P_{\boldsymbol{k}_2}, \qquad (11)
$$

with $P_{\boldsymbol{k}} = \sum_{n\in\mathrm{occ.}} |u_n(\boldsymbol{k})\rangle\langle u_n(\boldsymbol{k})|$ the projector on the occupied subspace of a Hamiltonian. The Wilson loop is inherently gauge invariant due to the gauge invariance of the projector $P_{\boldsymbol{k}}$. The Berry phase associated with the loop is given by the determinant of the Wilson operator $\det(\mathscr{W}) = \exp(\mathrm{i}\phi_{\mathrm{B}})$. If the Hamiltonian has a symmetry R, it can be shown that[77]

$$
\tilde{R}\mathscr{W}_{\boldsymbol{k}_1\boldsymbol{k}_2}\tilde{R}^{-1} = \mathscr{W}_{R\boldsymbol{k}_1 R\boldsymbol{k}_2}, \qquad (12)
$$

with R acting in reciprocal space and $\tilde{R}$ in occupied band space. The symmetry expectation value of Wilson loop eigenstates $|v_i\rangle$ is calculated as $\langle v_i|\tilde{R}|v_i\rangle$.

For Weyl[11] and Dirac[76] semimetals it is known that the Wilson loop spectrum on a sphere enclosing the semimetallic point gives the topological classification of the crossing. Also in our case with TPs, a similar kind of topological classification is possible. Here the classification is demonstrated with a tight-binding model of ZrTe obtained in Ref. [21].

In Fig. 8(a), we show a spherical surface on which the Wilson loop spectrum is to be evaluated. The sphere is chosen such that the Hamiltonian is gapped everywhere on the surface, the symmetry axis containing the TPs goes through the center of the sphere and both TPs are enclosed by the sphere. The latter point is important, since there is always at least one nodal line connecting two TPs, therefore including only one TP would not fulfill the requirement that the Hamiltonian is gapped on the sphere. Note that the Wilson lines are oriented such that the symmetry axis goes through their center. In Fig. 8(c), we plot the phases ϕ_i of the individual Wilson loop eigenvalues as a function of the azimuthal angle θ. The tight-binding model has 8 occupied states, therefore, we obtain 8 Wilson loop eigenvalue phases ϕ_i. Six ϕ_i (marked in black) are trivial and stay very close to 0 (2π), but two (marked in red and blue) seem to cross. Note that the σ_v symmetry constrains the ϕ_i such that the Wilson loop spectrum is mirror symmetric $\phi_i = -\phi_j$.[27] Since the Hamiltonian is gapped on the surface, and the Wilson loop is gauge invariant, the individual ϕ_i change smoothly with θ. Therefore, the connectivity of the ϕ_i can be determined as long as they are not degenerate. To obtain the connectivity across the degeneracy point between the red and blue Wilson eigenvalues, we calculate the C_3 symmetry expectation values of the corresponding states in Fig. 8(d). The grey dashed line in Fig. 8(d) indicates the position of the

crossing of the blue and red lines in Fig. 8(c). Note that the crossing of red and blue lines in Fig. 8(d) is accidental and we find that it can be avoided via choosing a cigar-shape, rather than a sphere. However, the C_3 symmetry expectation value is nondegenerate at the crossing in Fig. 8(c) and we can use Fig. 8(d) to unambiguously determine the connectivity for all θ. Therefore, the red and blue lines in the Wilson loop spectrum clearly indicate two hidden Berry curvature fluxes, one inward and one outward, through the sphere. The fluxes can be separated in the Wilson loop eigenbasis, corresponding to individual Chern numbers[78] of ± 1. The difference of the two individual Chern numbers divided by two constitutes a $\mathbb{Z}_2$ topological invariant for the TPs.

At the polar regions $\theta \approx 0$ or $\theta \approx -\pi$, the Wilson loop commutes with the C_3 symmetry due to Eq. (12). In this case, the C_3 expectation value in Fig. 8(d) is one of the possible C_3 eigenvalues $\{-1, \exp(\mathrm{i}\pi/3), \exp(-\mathrm{i}\pi/3)\}$, which are the starting and ending points of the lines in Fig. 8(d). Note that the 6 trivial ϕ_i (black dots) are almost fixed to the C_3 eigenvalues, whereas the 2 nontrivial ϕ_i (red/blue dots) change the C_3 eigenvalue from $\{-1, -1\}$ to $\{\exp(\mathrm{i}\pi/3), \exp(-\mathrm{i}\pi/3)\}$. Responsible for this behavior are the two valence bands having the rotational eigenvalues $-1, -1$ for k_z to the left of the two TPs and $\exp(\mathrm{i}\pi/3), \exp(-\mathrm{i}\pi/3)$ for k_z to the right of the two TPs. Therefore, the planes above G_1, G_2 are topologically distinct from the planes below, consequently uncovering the existence of crossing points realized as the two TPs here.

In Fig. 8(b), we give an example of a topologically trivial pair of TPs. In this case, the C_3 eigenvalues of the valence bands are the same to the left and to the right of the two TPs and hence the Wilson loop spectrum is in general gapped with an even $\mathbb{Z}_2$ invariant.

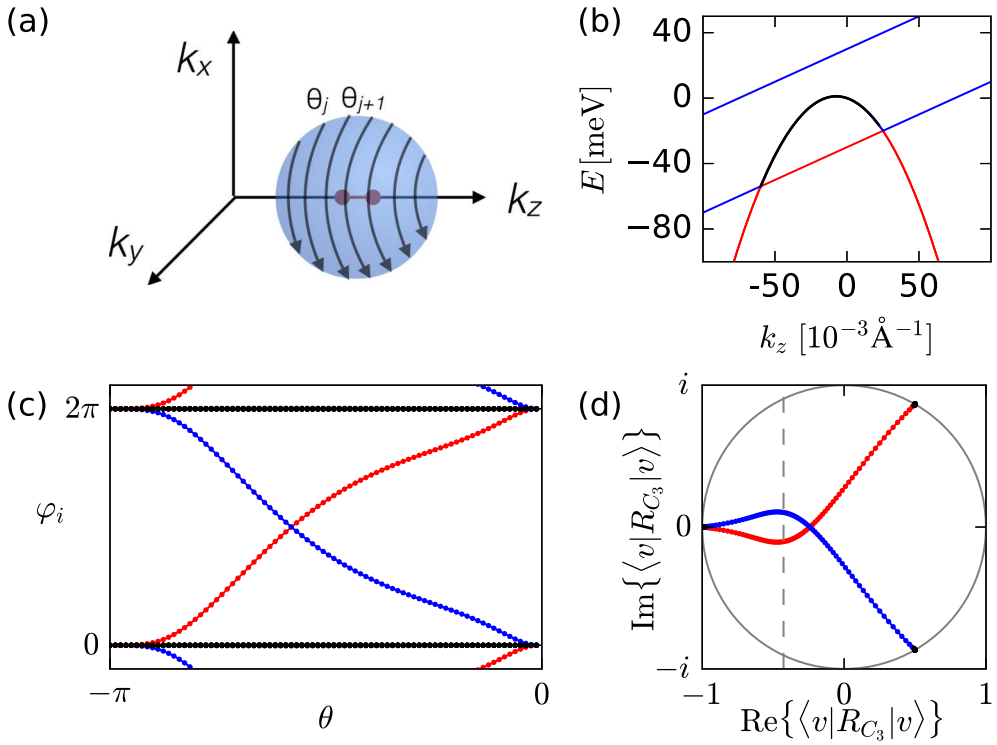


Fig. 8. (a) Pair of TPs (red points) connected by a nodal line (red line) enclosed by a sphere. The arrows indicate the individual Wilson loops winding around the sphere. (b) Example of a trivial pair of TPs. (c) The Wilson loop spectrum on a sphere enclosing a pair of TPs. Two Wilson loop eigenvalues feature gapless flows (colored in red and blue). (d) The C_3 symmetry expectation value of individual Wilson lines. Figure reused from Ref. [21].

4.3. Lifshiftz transitions

Using the models of Eqs. (5) and (10), we can analyze the Lifshitz transitions of Fermi surfaces in the TPTMs. The nodal lines of Figs. 2(a) and 2(b) guarantee that several Fermi surfaces touch within a finite energy window in between two TPs. Figure 9(a) illustrates the fixed $k_y = 0$ cuts of the Fermi surface for the Fermi level E_F placed above, below, and in between the two TPs, representing three topologically distinct Fermi surfaces. At each of the two TPs, a topological Lifshitz transition takes place: one of the Fermi pockets shrinks to a point reopening either inside or outside another Fermi pocket. When E_F is placed in between the two TPs, there appears a topologically protected touching point between electron and hole pockets, similar to the type-II WP scenario.[11]

The Lifshitz transitions occurring in type-B TPTMs are illustrated in Fig. 9(b). The difference to the type-A transitions is that a single touching point between the Fermi pockets (the point of quadratic band touching) now splits into four points (or two linear band touchings on each mirror plane) due to the

breaking of σ_h (see insets of Fig. 9(b)). Intricate spin textures with changing winding numbers were predicted for a (111)-strained HgTe in Ref. [43], which according to the classification is a type-B TPTM. Nontrivial windings in the spin-texture are also found for type-A TPTMs.[22]

Since the distinct Fermi pockets touch in TPTMs for a range of energies, the topological charge of individual pockets is undefined. However, as mentioned above, this degeneracy is lifted via breaking σ_v by, for example, applying a small Zeeman field in the z direction or photoirradiation effects.[79] In this case, each of the TPs splits into two WPs with opposite Chern numbers as illustrated in Fig. 9(c). The touching Fermi pockets now separate, and well-defined Chern numbers can be assigned to each of them, see Fig. 9(d). The Chern number of a pocket is equal to the summed up chiralities of WPs enclosed within it.

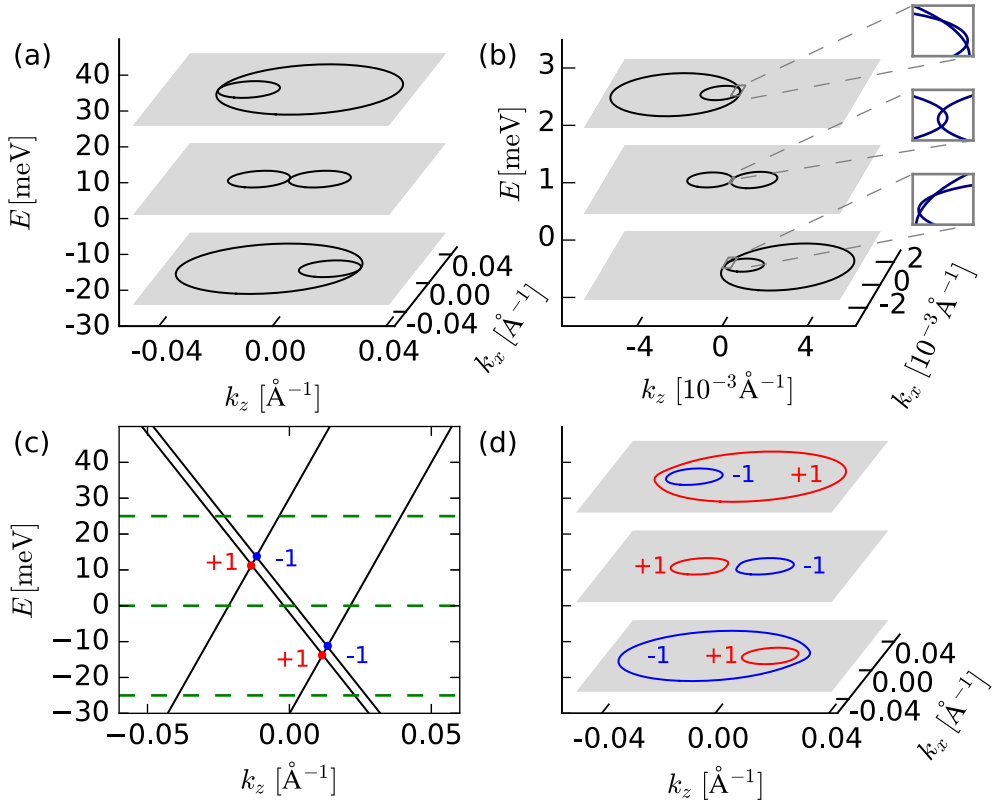


Fig. 9. Fermi surfaces for (a) type-A and (b) type-B triple-point topological metals at three different energy cuts: below, between, and above the two triple-points. The three small insets in panel (b) show that for the type-B scenario, there are several distinct touching points between the Fermi pockets. (c) Band structure around the triple-points for a small Zeeman field parallel to the C_3 axis. (d) Fermi surface of type-A triple-point topological metal with a small Zeeman field. In panels (c) and (d), the Chern numbers of WPs and Fermi surfaces are marked in red (+1) and blue (−1). Figure reused from Ref. [21].

4.4. Surface states

Here we use the previously defined $\boldsymbol{k}\cdot\boldsymbol{p}$ models to gain insights into the first-principles surface states shown in Section 3. The $\boldsymbol{k}\cdot\boldsymbol{p}$ surface state calculations are facilitated by discretizing the momentum perpendicular to the surface, and thus generating a one-dimensional (1D) tight-binding model with the parallel momenta as auxilliary parameters.[80] The SDOS is then calculated using the iterative Green's function method.[81,82] For the $\boldsymbol{k}\cdot\boldsymbol{p}$ models given in Eqs. (3) and (4), we use 1 Å as the discretization length and 2 Å for Eq. (7).

We use the $\boldsymbol{k}\cdot\boldsymbol{p}$ models with parameters that fit the band structure of ZrTe. The model around A, given in Eq. (3), is characterized by the mirror Chern numbers $C_{m=\pm i} = \mp 1$ in the $k_z = \pi$ plane. Therefore, a topological-insulator-like surface state is expected on a surface orthogonal to the σ_h mirror plane. In Fig. 10(a), we show the SDOS on a surface orthogonal to y, corresponding to the (010) surface in the WC structure. On the k_x axis, the upper topologically nontrivial surface state emerges from the conduction bands and connects to the valence bands. There is another trivial surface state with opposite mirror eigenvalue below. If we compare this to the first-principles surface states shown in Fig. 4(k), then these two surface states will form a Dirac cone at $\overline{R}$ for the Te-terminated surface. In Fig. 10(b), the Fermi surface is plotted. The topologically nontrivial hole pockets are connected by a pair of Fermi arcs.

The $\boldsymbol{k}\cdot\boldsymbol{p}$ model around K is characterized by a total Chern number of $C = 1$, while $C = -1$ at K'. Hence around K and K', a quantum Hall like surface state is expected. This is confirmed in Figs. 10(c) and 10(d), where we calculate the SDOS on a surface orthogonal to y. The surface states give an excellent match to the first-principles result presented in Figs. 4(j)

and 4(k).

We now want to take a closer look at the surface states of TPs. Generally, one can distinguish two different scenarios. The first one corresponds to a pair of TPs that are very close together, i.e., the inversion symmetry breaking is small. Then one cannot discriminate which of the two TPs is the source of a Fermi arc and consequently the Fermi arcs have the characteristics of a Dirac semimetal like in the CuPt-ordered $InAs_{0.5}Sb_{0.5}$ case, see Fig. 7(f).[20] In the other scenario, one deals with isolated or a well separated pair of TPs. Here it is more useful to consider each TP as two degenerate Weyl nodes with opposite chirality, see Fig. 9(c). In this case, it is natural that each TP has two Fermi arcs connecting with their neighbors (it is also possible that the two WPs themselves are connected by a Fermi arc which vanishes when they form a TP).[45] This scenario corresponds to the TPs in WC-like structures and in half-Heuslers.

It is insightful to look at the evolution of Fermi arcs from Dirac semimetal to TPTM. In a $\boldsymbol{k}\cdot\boldsymbol{p}$-model for ZrTe proposed in Ref. [21], one can easily tune between inversion symmetric and asymmetric band structures. In Fig. 11, we compare the surface states obtained from this model with and without

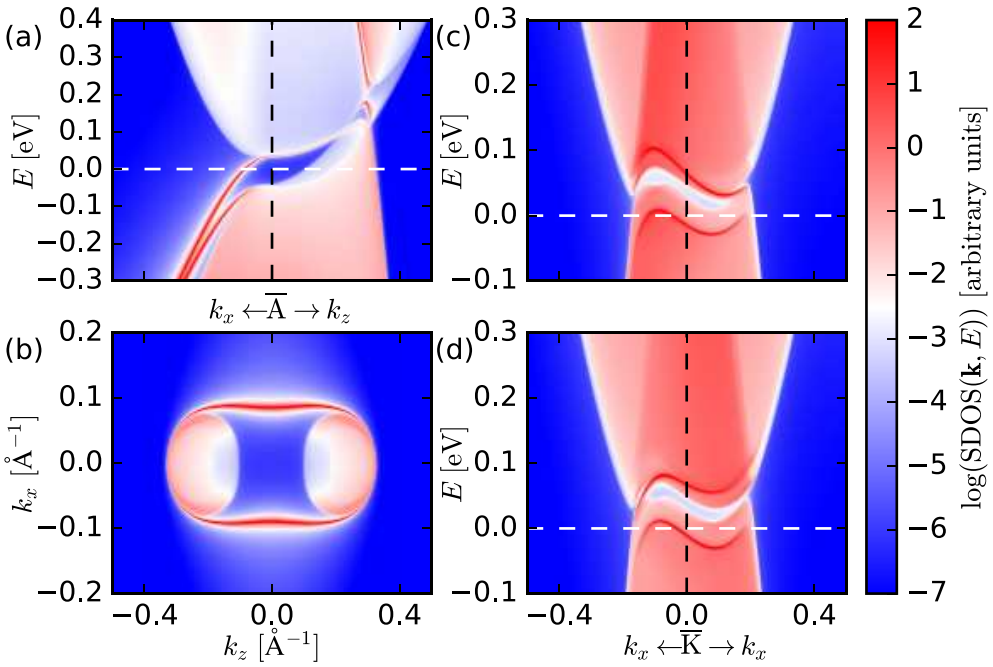


Fig. 10. SDOS of the (010)-surface for the $\boldsymbol{k}\cdot\boldsymbol{p}$ models given in Eqs. (3) and (7). (a) and (b) The SDOS and Fermi surface around the $\overline{A}$ point. (c) (d) The SDOS around the $\overline{K}$ point for the (c) top and (d) bottom surfaces. Figure reused from Ref. [21].

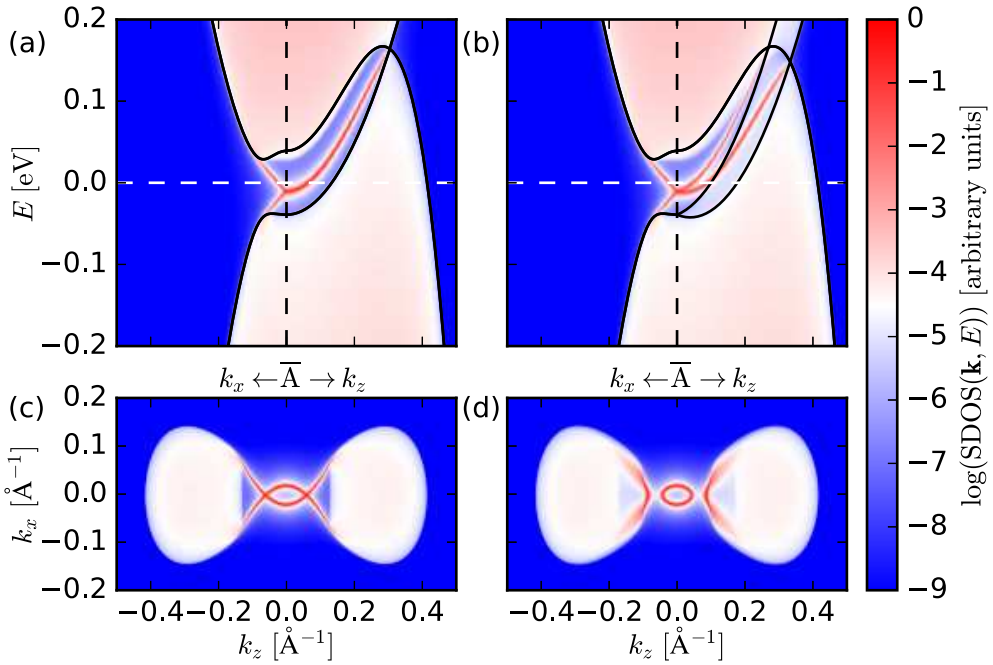


Fig. 11. Surface states on the (010)-surface obtained from a $\boldsymbol{k}\cdot\boldsymbol{p}$ model for ZrTe with Eq. (4). (a) The surface density of states (the black lines show the bulk dispersion for $k_y = 0$) and (c) the surface Fermi surface with inversion symmetry (those without inversion symmetry are shown correspondingly in (c) and (d)). Figure reused from Ref. [21].

inversion symmetry. In the presence of inversion and TR symmetries, the two TPs merge into a four-fold degenerate Dirac point. Across all energies in the gap, the two hole pockets around $\overline{A}$ are connected by two Fermi arcs and the surface state on the k_z-axis is two-fold degenerate. Breaking of inversion symmetry then splits the Dirac point into two TPs. Each TP contributes a single non-degenerate surface state. Since the two surface states are split along the k_z-axis, the Fermi arcs are not required to connect the two hole pockets. Instead, one finds a topological-insulator-like Dirac cone around $\overline{A}$ which is still protected by TR and σ_h symmetries.

4.5. Magnetotransport

The topologically non-trivial nature of Weyl semimetals reveals itself most spectacularly in the so-called chiral anomaly of the quantum field theory, realized in negative magnetoresistance measurements.[30,83–88] The chiral anomaly effect was originally proposed in high-energy particle physics, where it was referred as the Adler–Bell–Jackiw anomaly.[30,83–87] Weyl semimetals provide an excellent platform to study the chiral anomaly effect in condensed matter systems. In presence of a parallel magnetic ($\boldsymbol{B}$) and electric field ($\boldsymbol{E}$), the resistivity of Weyl semimetals decreases (i.e. conductivity increases) with increasing $\boldsymbol{B}$-field in a finite range. This phenomenon is related to the chiral anomaly, and is generally referred as negative magnetoresistance. Although magnetoresistance is known to be positive in most of the known topologically trivial materials, negative magnetoresistance is quite rare. Negative magnetoresistance has been experimentally observed in several topologically non-trivial systems having non-zero Berry curvature near the Fermi-level.[89–94] Here, it is important to note that negative magnetoresistance could also appear in topologically trivial systems through giant magnetoresistance effect and/or current-jetting effect.[93,95]

In a Weyl semimetal, when an external $\boldsymbol{B}$-field is applied parallel to an $\boldsymbol{E}$-field that is orientated along a momentum direction connecting two opposite Weyl nodes, a chiral Weyl charge imbalance occurs. The applied $\boldsymbol{B}$-field induces a charge pumping from one Weyl node to another Weyl node having opposite chirality separated in momentum space along the $\boldsymbol{B} \parallel \boldsymbol{E}$ direction. This charge pumping process breaks the conservation of chiral charge, however, it retains the total charge conservation. The rate of charge pumping (W) between two opposite Weyl nodes can be described by equation[86,96]

$$W = \chi \frac{e^3}{4\pi^2\hbar^2} \boldsymbol{E} \cdot \boldsymbol{B}, \tag{13}$$

where χ, $\hbar$, and e denote the chirality of the Weyl nodes (± 1), the reduced Planck's constant, and the electron charge, respectively. The charge pumping process eventually saturates via inter-Weyl node scattering,[86] and a net chiral current is generated. The generation of this additional current causes enhanced conduction that increases with increasing $\boldsymbol{B}$-field, and hence yields negative magnetoresistance.[91,97,98] The chiral current conductivity is usually proportional to $\boldsymbol{B^2}$ in low field range.[86,96]

Since the chiral charge pumping rate is proportional to $\boldsymbol{E} \cdot \boldsymbol{B}$, negative magnetoresistance is expected to vary with the changing $\boldsymbol{E}$ and $\boldsymbol{B}$ field directions. However, if negative magnetoresistance is too sensitive to the relative orientation of $\boldsymbol{E}$ and $\boldsymbol{B}$ fields (i.e., it disappears after changing the relative angle between $\boldsymbol{E}$ and $\boldsymbol{B}$ field directions by 1°–2°), it might not be a signature of the chiral anomaly effect, rather it could originate from the classical current jetting effect.[93,95] The current jetting effect is a geometric effect which occurs when the current forms jets flowing along the high conduction directions in materials having large conductance anisotropy.[93] Therefore, it is important to carefully check the origin of negative magnetoresistance in topological materials.

Large negative magnetoresistance has been observed in Dirac/Weyl semimetals and in triple-point metals.[90,93,97–108] In Dirac semimetals or in triple-point metals, a Dirac point or a triple-point, respectively, splits into a pair of Weyl points in presence of a magnetic field, which gives rise to negative magnetoresistance under strong $\boldsymbol{B}$ field ($\parallel \boldsymbol{E}$) at low temperatures. Type-I Weyl points produce a gapless Landau level spectrum in a magnetic field, whereas type-II Weyl points have an anisotropic chiral anomaly,[11] where the Landau level spectrum is gapless only for certain directions of the applied magnetic field. Therefore, the negative magnetoresistance is strongly anisotropic in type-II Dirac/Weyl semimetals, as observed in type-II Dirac semimetal $PtSe_2$[96] and in type-II Weyl semimetal WTe_2.[106,108–110] Therefore, the magnetotransport properties of TPs primarily depend on the direction of the applied magnetic field. A C_3 symmetry preserving magnetic field (along the C_3-axis) does not gap the Landau level spectrum of a TP, but instead each TP contributes a single chiral Landau level (see Fig. 12). However, if the field is applied in a C_3-breaking direction, the Landau level spectrum becomes gapped. Such a directional dependence also occurs in Dirac semimetals.[111]

The Landau levels are obtained by performing a Peierls substitution of k_x and k_y in the $\boldsymbol{k} \cdot \boldsymbol{p}$ Hamiltonian by $k_x = \frac{\mathrm{i}}{\sqrt{2}l_B}(a^\dagger - a)$ and $k_y = \frac{\mathrm{i}}{\sqrt{2}l_B}(a^\dagger + a)$, with $l_B = \sqrt{\frac{\hbar}{eB}}$ the magnetic length and $a^\dagger$, a the raising and lowering operators, $a^\dagger|n\rangle = \sqrt{n+1}|n+1\rangle$ and $a|n\rangle = \sqrt{n}|n-1\rangle$. In Fig. 12, we show the Landau level spectra of CuPt-ordered $InAs_{0.5}Sb_{0.5}$ and ZrTe.[20,21] When the magnetic field is turned on, a pair of TPs turns into two crossing chiral Landau levels with opposite chirality. Due to the gapless Landau level spectrum, strong signatures of the TPTM state are observable in magnetotransport. Analogous to the chiral anomaly, one can create a $\mathbb{Z}_2$

anomaly by applying parallel magnetic and electric fields.[112]

Magnetotransport experiments in the TPTM WC confirm the presence of direction dependent negative magnetoresistance for parallel magnetic and electric fields.[34] Due to the material growth constraints, the longitudinal magnetoresistance has been only measured in directions orthogonal to the (001) axis. Further investigations are required to confirm that the negative magnetoresistance stems from the TPs. We refer the reader to Refs. [93], [113], and [94] for a more comprehensive review on the transport property of topological semimetals.

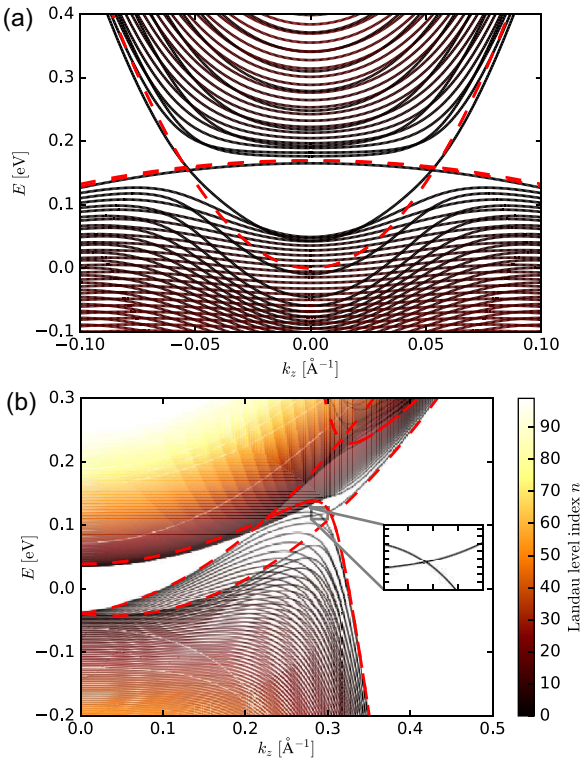


Fig. 12. (a) Landau levels in CuPt-ordered $InAs_{0.5}Sb_{0.5}$ with a magnetic field of 50 T applied parallel to the C_3 axis using the $\boldsymbol{k}\cdot\boldsymbol{p}$-model of Eq. (9) and (b) those in ZrT with a magnetic field of 20 T applied parallel to the C_3 axis using the $\boldsymbol{k}\cdot\boldsymbol{p}$-model of Eq. (3). The dashed red lines show the bulk bands. Figure adapted from Refs. [20] and [21].

In addition to the negative magnetoresistance, the topological non-trivial features of electronic bandstructure and Fermi-surface are manifested in distinct quantum oscillations in the resistivity (ρ) data at strong $\boldsymbol{B}$-field. Under the application of a strong $\boldsymbol{B}$-field, the electronic bandstructure evolves into a set of 1D Landau levels, as shown in Fig. 12, and these Landau levels yield quantum oscillations (Shubnikov–de Haas oscillations) in the $\rho(\boldsymbol{B})$ data at low temperatures. These oscillations can be described using Lifshitz–Kosevich formula[114,115] $\rho \sim \cos[2\pi(F/B+\phi)]$, where F and ϕ represent the oscillation frequency and phase shift, respectively. Depending upon the topological nature and morphology of the Fermi-surface, ϕ could attain different values. For topologically trivial materials having parabolic band dispersion near the Fermi-level (i.e., zero Berry phase), $\phi = \pm 1/2$ (in 2D) and $\pm 5/8$ (in 3D). Here $+/-$ refers to hole/electron carriers. In case of Dirac/Weyl semimetals, the linearly dispersing bands near the Dirac/Weyl points inherit π Berry phase, which results inphase shifts of $\phi = 0$ (in 2D) and $\pm 1/8$ (in 3D).[30,116–119] TPTMs are hybrid between Dirac and Weyl semimetals, hosting a topologically non-trivial nodal line near the Fermi-level, therefore an anisotropic phase shift which is sensitive to the orientation of the Fermi-surface cross-section and $\boldsymbol{B}$-field is expected. An electron traversing along a closed path parallel to the nodal line plane, or along a perpendicular circle enclosing the nodal line, could acquire a Berry phase of 0, or π, respectively.[120] Hence, different phase shifts ($\phi = \pm 1/8$ or $\pm 5/8$) could be observed depending upon the direction of the $\boldsymbol{B}$-field and Fermi-surface cross-section. An excellent discussion related to the quantum oscillations and ϕ values for different topological semimetals can be found in Ref. [115].

5. Topology of phonons in triple-point metals

After describing the topological electronic properties of triple-point-metals, we shift our focus to the topological vibrational properties of these compounds. The concept of topology from the electronic bandstructure has been successfully extended to the vibrational bandstructure of materials.[121–125] In recent works, topologically protected band-crossings have been reported in the phonon spectrum of solid state crystals.[42,126–129] Soon after the theoretical prediction of double-Weyl phonons in the phonon spectrum of transition-metal monosilicides MSi (M = Fe, Co, Mn, Re, Ru),[126] Miao *et al.*[130] experimentally reported the first observation of double Weyl points in FeSi by means of inelastic x-ray scattering measurements. This paved the way for realization of novel phononic (bosonic) quasiparticle excitations and the associated topological properties in condensed matter systems. Several other studies focused on the topology of phonons in model systems, and predicted novel quantum phenomena arising due to the non-trivial topology of phonons, such as quantum Hall conductance, quantized phonon Berry phase, topologically protected pseudo spin-polarized interface states, phonon pseudospin Hall effect, valley effects of phonons, realization of phonon diode, and topological acoustics.[131–141] Recently, topologically protected Weyl nodal lines have been predicted in the phonon spectrum of bulk MgB_2.[129]

Analogous to the physics of the electronic bandstructure, a nontrivial band-inversion between the low frequency acoustic and high frequency optical phonon modes results in topologically protected phonon band-crossings in the momentum space. Low frequency excitations of phonons near these topological band-crossing points could yield features of novel bosonic quasiparticles, such as Dirac, Weyl, and/or

triple-point. Here, one main difference from the electronic structure stems from the fact that phononic excitations have bosonic character, whereas low-energy electronic excitations are fermionic. This rules out the applicability of the Pauli's exclusion principle on phononic excitations in crystalline solids. In addition to the crystalline systems, topological bosonic quasiparticles have been realized in the photonic systems, metamaterials, and optical lattices.[142–151] Moreover, Süsstrunk and Huber reported that oscillations of a simple pendulum in classic mechanical systems could also host topological bosonic modes.[123–125]

Although Dirac and Weyl phonon modes have been known since the last decade,[152] triple-point phonons joined the family of topological phonons only in 2018.[42,128] In Refs. [128] and [42], the existence of triple-point phonons was predicted in several special type-A triple-point metals having C_{3v} symmetry, such as ZrTe, HfTe, TiS, TaSb, and TaBi. Notably, these materials also host Weyl fermions and triple-point fermions in their electronic spectra. These binary compounds belong to space group #187 ($P\bar{6}m2$) having 2 atoms in the primitive cell and thus, inheriting three acoustic and three optical branches in their phonon spectrum. When the mass difference ($\Delta m = M - m$, where $M > m$) between the constituent atoms is large, the direct frequency band gap between the optical and acoustic branches (Δ_g) is finite and positive at the $A(0, 0, \pi/c)$ point of the hexagonal Brillouin zone. With decreasing Δm, the frequency band gap decreases systematically, and acoustic and optical phonon bands invert in the frequency space for certain binary compounds having small Δm. A necessary condition for such phonon band-inversion is[42]

$$\Delta_g = \sqrt{\frac{2\beta_{\parallel}}{m}} - \sqrt{\frac{2\beta_{\perp}}{M}}. \tag{14}$$

Here, Δ_g is the direct frequency band gap at the $A(0, 0, \pi/c)$ point of the Brillouin zone, $\beta_{\parallel}$ and $\beta_{\perp}$ are in-plane and out-of-plane second-order interatomic force constants between the atoms of masses m and M, respectively.

Figure 13(a) shows the calculated phonon spectra of TaX (X = N, P, As, Sb) binaries having Δm in decreasing order.[42] As the X atom in TaX gets heavier, the frequency of the optical phonon modes lowers, causing a systematic decrease in the frequency bandgap with decreasing Δm, and a phonon band-inversion takes place in TaSb along the Γ–A direction of the Brillouin zone, where two degenerate optical phonon modes acquire lower frequency than a non-degenerate acoustic phonon mode. This phonon band-inversion results in a gapless

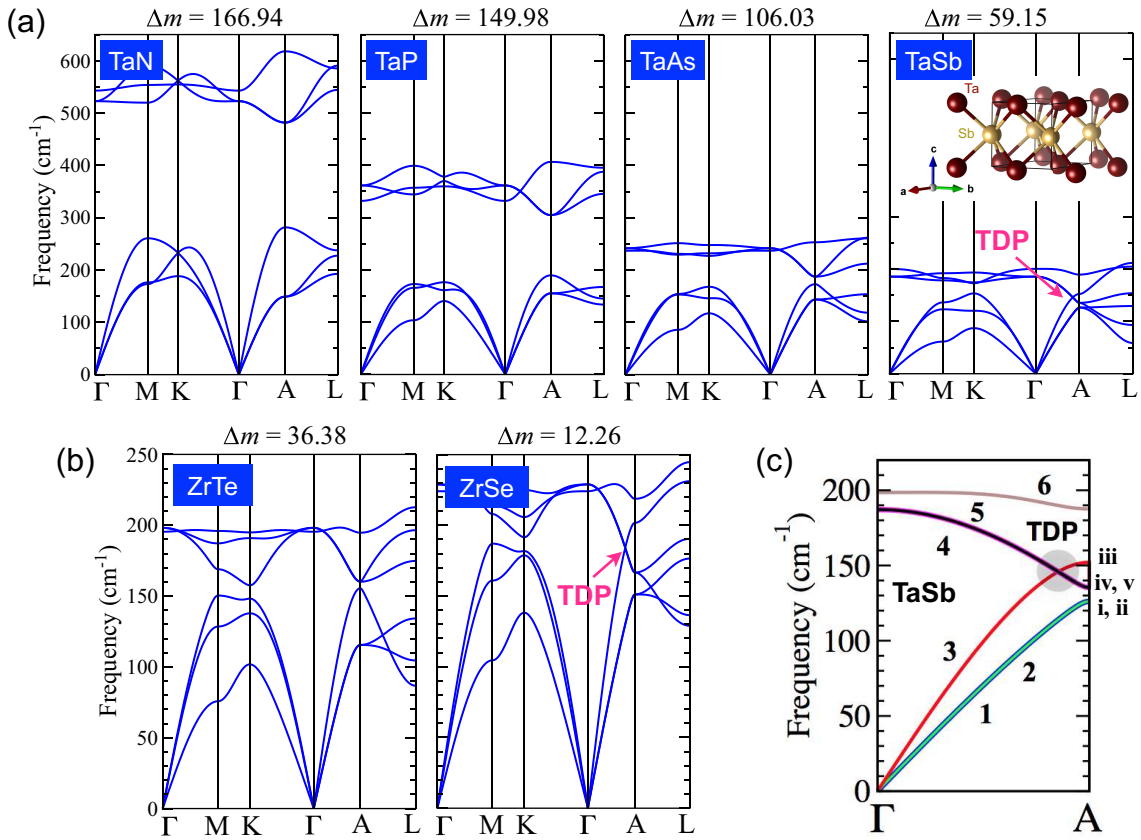


Fig. 13. Phonon dispersion of (a) TaX (X = N, P, As, Sb) and (b) ZrY (Y = Se, Te) binaries calculated using the density functional perturbation theory (DFPT) for supercell of size $2 \times 2 \times 2$. The mass difference Δm is provided in units of g/mol. A prototype crystal structure of TaSb is given in the inset. The primitive unit cell contains one Ta and one X (Sb) atom at (2/3, 0.0, 2/3) and (0.0, 1/2, 0.0) sites, respectively. TDP is marked in the phonon spectrum of TaSb and ZrSe along the Γ–A path. (c) An enlarged view of phonon dispersion in TaSb along Γ–A path. Colors and numbers depict distinct phonon modes. Arabic (Roman) numerals are used to mark phonon modes before (after) the band-inversion. Some data from Ref. [42] have been reused to produce this figure.

triply degenerate point (TDP) in the phonon spectrum of TaSb at frequency ~ 145 cm^{-1} at $q = (0, 0, 0.428)$. This point is marked in Fig. 13(a). As shown in Fig. 13(b), a similar mass induced phonon band-inversion also occurs in ZrY (Y = Se, Te) family. ZrY binaries are isostructural and isoelectronic to TaX.[128] In ZrTe, there exists a finite positive Δ_g due to the relatively large Δm. Whereas, the net frequency gap closes in ZrSe, which has relatively smaller Δm, and Δ_g becomes negative at the A-point due to the observed phonon band-inversion along the Γ–A path.

An enlarged view of the phonon dispersion along the Γ–A direction of TaSb is shown in Fig. 13(c). In this figure, the degeneracy of phonon modes and formation of a TDP can be clearly observed. Another TDP is located in other direction in the Brillouin zone at the same C_{3v}-symmetric line. The two degenerate optical phonon modes participating in the phonon band-crossing at TDP correspond to the in-plane (x–y) optical vibrations of atoms, whereas the non-degenerate acoustic mode involved in the phonon band-crossing at TDP belongs to the out-of-plane (z) acoustic vibration of atoms. The competition between in-plane and out-of-plane interatomic force constants and Δm are the primary reason of the phonon-band inversion in TaSb and ZrSe.[42]

We note that the same methods[48,76] that are used to compute the topological character of electronic band-crossings can also be employed to evaluate the topology of phonon band-crossings. However, it turns out that capturing the topology of phonon band-crossings is different from that of the electronic case. In case of non-interacting electronic systems, we analyze the symmetrized Hamiltonian of system for topological classification of the studied system, whereas, the topological classification of phononic systems can be built using the dynamical matrices $D(\boldsymbol{q})$.

Similar to the case of triple-points in the electronic spectrum,[21] gapless TDPs in the phonon spectrum are connected by a gapless nodal line in the phonon frequency space. This nodal line, shown in Fig. 14(d), is formed by the degenerate optical phonon modes near the TDP, and it is being protected by the C_{3v} rotational symmetry of the crystal. Under the C_{3v} symmetry, the xx and yy interatomic force constants transform just like the p_x and p_y orbitals in C_{3v} group, forming a 2D irreducible representation E, which enforces the degeneracy of the optical phonon modes along Γ–A. Computation of Berry phase (ϕ_B) using the Wilson loop approach along path S^1, as shown in Fig. 14(d), reveals $\phi_B = 0$ for the gapless nodal line connecting two TDPs.[42]

In order to reveal the topology of a TDP, one can split the two connected TDPs by breaking the C_{3v} symmetry. This can be done by changing the xx and yy entries in $D(\boldsymbol{q})$, which is equivalent of tuning the interatomic force-constants (or equivalently, classical spring constants) between atoms along x and y directions.[42] This trick lifts up the degeneracy of the optical phonon modes, as shown in Figs. 14(b) and 14(c), and enables us to probe the topological nature of TDP. It is worth noting that the aforementioned trick does not destroy the gapless nodal line, rather it results in a gapless nodal loop formed by the inverted optical and acoustic phonon bands (see Figs. 14(e) and 14(f)). We can now define a path S^2 (and S^3) enclosing the gapless nodal loop, and compute the ϕ_B using the Wilson loop as demonstrated in Figs. 14(e) and 14(f). This calculation results in $\phi_B = \pi$ for S^2 and S^3 paths, thus confirming the topological nature of the TDP.[42] The mentioned technique is analogous to splitting two triple-point nodes in the electronic spectrum into four Weyl nodes by applying a Zeeman field.[21]

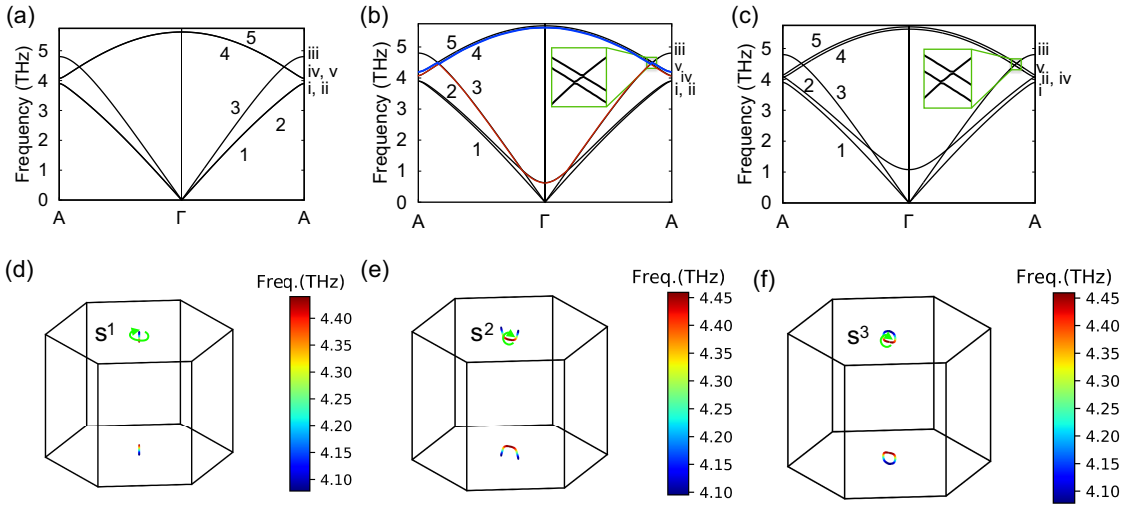


Fig. 14. (a) The phonon spectrum of TaSb along the C_{3v}-symmetric line of the Brillouin zone: doubly degenerate phonon bands (4,5) and (iv,v) can be seen. (b) The phonon spectrum of TaSb with the xx and yy force constants in the dynamical matrix made unequal for Ta. The degeneracy of (4,5) and (iv, v) is lifted. (c) The phonon spectrum of TaSb with the xx and yy force constants in the dynamical matrix made unequal for Sb. The degeneracy of (4,5) and (iv, v) is lifted. (d) The non-topological open nodal line formed in the BZ by bands iv and v of panel (a). The loop S^1 encircles this line, but $\phi_B(S^1) = 0$. (e) The closed nodal loop formed by bands iv and v in the BZ for the case of panel (b) away from the Γ–A line. The contour S^2 links with this loop and $\phi_B(S^2) = \pi$. (f) The closed nodal loop formed by bands iv and v in the BZ for the case of panel (c). For a contour S^3 linked with this loop, $\phi_B(S^3) = \pi$. Figure adopted from Ref. [42] with permission.

The nontrivial topology of phonon band-crossings in bulk indicates the presence of nontrivial surface phonon states.[42] In fact, Li *et al.* predicted unusual phonon surface states (open gapless arcs) in TiS and HfTe compounds, which are triple-point metals hosting TDPs.[128]

6. Thermoelectricity in triple-point-metals

Since the nontrivial topology of electronic bands is often manifested in the electronic transport measurements, the phonon topology could have observable signatures in the lattice thermal transport measurements. It has been reported that topologically protected nontrivial phonon band-crossings introduce robust phonon-phonon scattering centers that enormously suppress the lattice thermal conductivity (κ_{ph}) in triple-point metals hosting TDPs.[42] In Fig. 15(a), we compare the κ_{ph} of two isostructural and isoelectronic triple-point metals TaN and TaSb, where the later hosts TDPs whereas the former does not. We notice that the overall κ_{ph} in TaSb is almost three orders in magnitude smaller than that in TaN. Such a large reduction in κ_{ph} causes a direct benefit towards the improved thermoelectric performance of triple-point metals hosting TDPs.[42]

The thermoelectric figure of merit, $ZT = \frac{S^2\sigma}{\kappa_{el}+\kappa_{ph}}T$, is the key indicator of the thermoelectric performance of any material. To achieve large ZT, one requires large thermopower or Seebeck coefficient (S), high electrical conductivity (σ), low electronic thermal conductivity (κ_{el}), and low lattice thermal conductivity (κ_{ph}) at a given temperature (T). Unfortunately, σ and κ_{el} are intrinsically coupled following the Wiedemann–Franz law, i.e., $\kappa_{el} = L_0 T\sigma$, where L_0 is the Lorenz number.[153] Therefore, an optimal balance is required between σ and κ_{el}. Another key factor is the thermopower or Seebeck coefficient (S) which is primarily governed by the electronic electronic density of states near the Fermi-level. Generally, narrow bandgap semiconductors (with small $\kappa_{el} + \kappa_{ph}$) exhibit the best thermoelectric performance ($ZT \sim 2$–3) when slightly doped by n- or p-type charge carriers.[153–158] Whereas, metals are known to be poor thermoelectrics due to their large σ and large κ_{el} (because of no energy bandgap). Moreover, κ_{ph} is also considerably large in most of the metals, thus, overall ZT is quite low in metals ranging from 0.0001 to 0.001.[159–161]

The triple-point metals hosting TDPs seem to be special metals having considerably large and sizable ZT. The maximum estimated ZT in triple-point metals hosting TDPs ranges from ~ 0.15 (at room temperature) to ~ 0.4 (at 800 K).[42] Remarkably, in HfTe (which is a triple-point metal hosting TDPs), the maximum estimated ZT ranges from 0.35 (at 300 K) to 0.42 (at 800 K) for electron doping (see Figs. 15(b) and 15(c)). Evidently, the thermoelectric performance of triple-point metals hosting TDPs is 2–3 orders in magnitude larger than that of the trivial metals.[42]

Two key factors combine to enhance the net ZT in triple-point metals. First, the presence of TDP, which gives rise to reduced κ_{ph}. Second, the nontrivial electronic band-crossings near the Fermi-level, i.e., the presence of gapless Weyl/triple-points fermions, yield large σ (unfortunately, κ_{el} is also large) as well as enhanced thermopower S. Notably, σ lies in the same order of magnitude ($\sigma/\tau \sim 10^{20}$ $\Omega^{-1}\cdot$ms^{-1} at low-doping concentrations, τ being the electron–phonon relaxation time) for all the yet studied triple-point metals.[42] Gapless points near the Fermi-level give rise to sharp enhancement in the electronic density of states near the Fermi-level, which increases S according to the Mahan–Sofo theory.[162] Thus, triple-point metals with TDPs inherit high S, high σ, and low κ_{ph}, which consequently yields relatively better thermoelectric performance in such metals. Figures 15(b) and 15(c) compare the thermopower (S) and thermoelectric performance (ZT) of selected triple-point metals with and without TDPs in their phonon spectra. For more technical details regarding the calculation of vibrational and thermoelectric properties, we recommend the reader to Ref. [42].

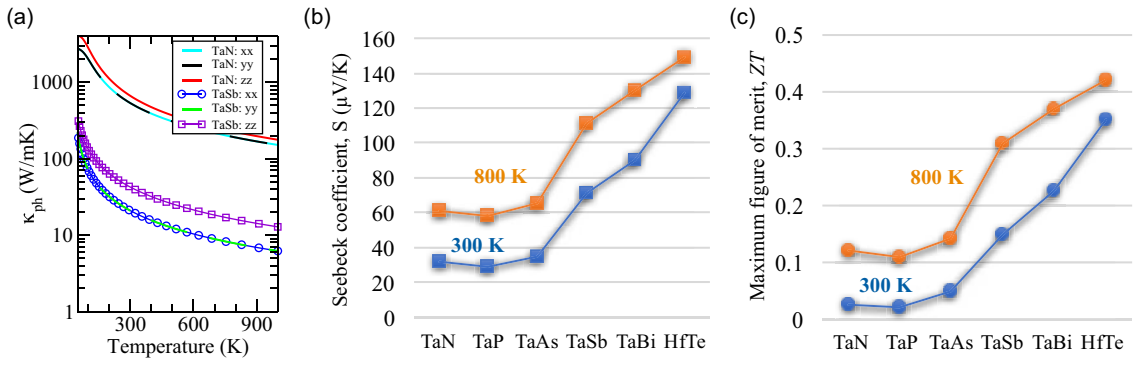


Fig. 15. (a) Comparison of the calculated lattice thermal conductivity κ_{ph} versus temperature data for TaN and TaSb binaries. Vertical axis is in logarithmic scale. (b) The maximum estimated thermopower or Seebeck coefficient, and (c) maximum estimated thermoelectric figure of merit computed at 300 K and 800 K for the electronic doping case. Data from Ref. [42] is reused to produce this figure.

7. Concluding remarks

We have overviewed the theoretical and experimental progress in the field of triple-point fermions protected by symmorphic symmetries. While the topological classification and basic band structure of triple-points are now well understood, open challenges lie ahead in investigating the transport and optical properties. In particular, low temperature applications could arise due to the presence of direction dependent magnetotransport.

Experimentalists are always in need of more accessible material candidates to confirm the manifold theoretical predictions. Recent experimental progress has been made for MoP,[36,37] where the existence of triple-points has been directly confirmed by ARPES, and WC,[34,35] of which the Fermi arcs and magnetotransport of triple-points have been investigated. To improve on this study, materials with good growth characteristics and well separated triple-points close to the Fermi level are desired. The recently predicted half-Heusler materials seem to have very favorable properties in this respect.[45]

Lastly, we have surveyed the topology of phonons in condensed matter systems, particularly in triple-point metals, and also discussed the numerical techniques required to evaluate the nontrivial topological nature of the triple-point nodes present in the phonon spectrum. The presence of topological phonon band-crossings usually introduces phonon–phonon scattering centers yielding low lattice thermal conductivity (phonon glass), whereas the presence of gapless topological nodes near the Fermi-level yields good electrical conductivity and thermopower (electron crystal). These two factors (electron crystal + phonon glass) combine to improve the thermoelectric performance of certain triple-point metals that host TDPs in their phonon spectra. Although the thermoelectric performance of triple-point metals is not comparable to that of the best known thermoelectrics (it is obviously expected given the metallicity), triple-point metals with topological phonon band-crossings rank much better when compared to ordinary metals in thermoelectricity.

To conclude, the discovery and description of triple-point metals will allow for further progress in understanding topological phenomena in solids and identification of topological materials with potential applications in technology. The triple-point fermion has been accepted as an integral part of the family of topological (semi-)metals.

Acknowledgments

Special gratitude goes to QuanSheng Wu, who made significant contributions to the understanding and illustration of the triple-point metal physics. We would also like to thank Z. Zu, J. Li, P. Krogstrup, and M. Troyer, with whom we collaborated on the fermionic part of our research. We acknowledge A. H. Romero and C. Yue, who made significant contribution to our study of the phonon topology. We also thank D. Gresch, T. Hyart, R. Skolasinski, J. Cano, J. W. Liu, C. M. Marcus, and M. Wimmer for useful discussions.

References

[1] Weng H M, Fang C, Fang Z, Bernevig B A and Dai X 2015 *Phys. Rev. X* **5** 011029
[2] Huang S M, Xu S Y, Belopolski I, Lee C C, Chang G, Wang B, Alidoust N, Bian G, Neupane M, Zhang C, Jia S, Bansil A, Lin H and Hasan M Z 2015 *Nat. Commun.* **6** 7373
[3] Xu S Y, Belopolski I, Alidoust N, Neupane M, Bian G, Zhang C, Sankar R, Chang G, Yuan Z, Lee C C, Huang S M, Zheng H, Ma J, Sanchez D S, Wang B, Bansil A, Chou F, Shibayev P P, Lin H, Jia S and Hasan M Z 2015 *Science* **349** 613
[4] Lv B Q, Weng H M, Fu B B, Wang X P, Miao H, Ma J, Richard P, Huang X C, Zhao L X, Chen G F, Fang Z, Dai X, Qian T and Ding H 2015 *Phys. Rev. X* **5** 031013
[5] Lv B Q, Xu N, Weng H M, Ma J Z, Richard P, Huang X C, Zhao L X, Chen G F, Matt C E, Bisti F, Strocov V N, Mesot J, Fang Z, Dai X, Qian T, Shi M and Ding H 2015 *Nat. Phys.* **11** 724
[6] Wan X, Turner A M, Vishwanath A and Savrasov S Y 2011 *Phys. Rev. B* **83** 205101
[7] Wang Z, Sun Y, Chen X Q, Franchini C, Xu G, Weng H, Dai X and Fang Z 2012 *Phys. Rev. B* **85** 195320
[8] Wang Z, Weng H, Wu Q, Dai X and Fang Z 2013 *Phys. Rev. B* **88** 125427
[9] Liu Z K, Jiang J, Zhou B, Wang Z J, Zhang Y, Weng H M, Prabhakaran D, Mo S K, Peng H, Dudin P, Kim T, Hoesch M, Fang Z, Dai X, Shen Z X, Feng D L, Hussain Z and Chen Y L 2014 *Nat. Mater.* **13** 677
[10] Xu S Y, Liu C, Kushwaha S K, Sankar R, Krizan J W, Belopolski I, Neupane M, Bian G, Alidoust N, Chang T R, Jeng H T, Huang C Y, Tsai W F, Lin H, Shibayev P P, Chou F C, Cava R J and Hasan M Z 2015 *Science* **347** 294
[11] Soluyanov A A, Gresch D, Wang Z, Wu Q, Troyer M, Dai X and Bernevig B A 2015 *Nature* **527** 495
[12] Wang Z, Alexandradinata A, Cava R J and Bernevig B A 2016 *Nature* **532** 189
[13] Kim Y, Wieder B J, Kane C L and Rappe A M 2015 *Phys. Rev. Lett.* **115** 036806
[14] Bzdušek T, Wu Q, Rüegg A, Sigrist M and Soluyanov A A 2016 *Nature* **538** 75
[15] Kruthoff J, de Boer J, van Wezel J, Kane C L and Slager R J 2017 *Phys. Rev. X* **7** 041069
[16] Wieder B J, Kim Y, Rappe A M and Kane C L 2016 *Phys. Rev. Lett.* **116** 186402
[17] Bradlyn B, Cano J, Wang Z, Vergniory M G, Felser C, Cava R J and Bernevig B A 2016 *Science* **353** aaf5037
[18] Burkov A A, Hook M D and Balents L 2011 *Phys. Rev. B* **84** 235126
[19] Parameswaran S A, Turner A M, Arovas D P and Vishwanath A 2013 *Nat. Phys.* **9** 299
[20] Winkler G W, Wu Q, Troyer M, Krogstrup P and Soluyanov A A 2016 *Phys. Rev. Lett.* **117** 076403
[21] Zhu Z, Winkler G W, Wu Q, Li J and Soluyanov A A 2016 *Phys. Rev. X* **6** 031003
[22] Weng H, Fang C, Fang Z and Dai X 2016 *Phys. Rev. B* **93** 241202
[23] Chang G, Xu S Y, Huang S M, Sanchez D S, Hsu C H, Bian G, Yu Z M, Belopolski I, Alidoust N, Zheng H, Chang T R, Jeng H T, Yang S A, Neupert T, Lin H and Hasan M Z 2017 *Sci. Rep.* **7** 1688
[24] Koster G 1963 *Properties of the Thirty-two Point Groups* Massachusetts institute of technology press research monograph M.I.T. Press)
[25] Aroyo M I, Orobengoa D, de la Flor G, Tasci E S, Perez-Mato J M and Wondratschek H 2014 *Acta Crystallogr. Sect. A* **70** 126
[26] Bradley C and Cracknell A 2010 *The Mathematical Theory of Symmetry in Solids: Representation Theory for Point Groups and Space Groups* EBSCO ebook academic collection (OUP Oxford)
[27] Alexandradinata A, Dai X and Bernevig B A 2014 *Phys. Rev. B* **89** 155114
[28] Chan Y H, Chiu C K, Chou M Y and Schnyder A P 2016 *Phys. Rev. B* **93** 205132

[29] Weng H, Liang Y, Xu Q, Yu R, Fang Z, Dai X and Kawazoe Y 2015 *Phys. Rev. B* **92** 045108
[30] Volovik G 2009 *The Universe in a Helium Droplet* International Series of Monographs on Physics (OUP Oxford)
[31] Mikitik G P and Sharlai Y V 2008 *Low Temp. Phys.* **34** 794
[32] Heikkilä T T and Volovik G E 2015 *New J. Phys.* **17** 093019
[33] Hyart T and Heikkilä T T 2016 *Phys. Rev. B* **93** 235147
[34] He J B, Chen D, Zhu W L, Zhang S, Zhao L X, Ren Z A and Chen G F 2017 *Phys. Rev. B* **95** 195165
[35] Ma J Z, He J B, Xu Y F, Lv B Q, Chen D, Zhu W L, Zhang S, Kong L Y, Gao X, Rong L Y, Huang Y B, Richard P, Xi C Y, Shao Y, Wang Y L, Gao H J, Dai X, Fang C, Weng H M, Chen G F, Qian T and Ding H 2018 *Nature Phys.* **14** 349
[36] Lv B Q, Feng Z L, Xu Q N, Gao X, Ma J Z, Kong L Y, Richard P, Huang Y B, Strocov V N, Fang C, Weng H M, Shi Y G, Qian T and Ding H 2017 *Nature* **546** 627
[37] Shekhar C, Sun Y, Kumar N, Nicklas M, Manna K, Suess V, Young O, Leermakers I, Foerster T, Schmidt M, Muechler L, Werner P, Schnelle W, Zeitler U, Yan B, Parkin S S P and Felser C 2019 *Nat. Commun.* **10** 2475
[38] Suchalkin S, Belenky G, Ermolaev M, Moon S, Jiang Y, Graf D, Smirnov D, Laikhtman B, Shterengas L, Kipshidze G, Svensson S P and Sarney W L 2018 *Nano Lett.* **18** 412
[39] Sun J P, Zhang D and Chang K 2017 *Chin. Phys. Lett.* **34** 027102
[40] Weng H, Fang C, Fang Z and Dai X 2016 *Phys. Rev. B* **94** 165201
[41] Sun J P, Zhang D and Chang K 2017 *Phys. Rev. B* **96** 045121
[42] Singh S, Wu Q, Yue C, Romero A H and Soluyanov A A 2018 *Phys. Rev. Mater.* **2** 114204
[43] Zaheer S, Young S M, Cellucci D, Teo J C Y, Kane C L, Mele E J and Rappe A M 2013 *Phys. Rev. B* **87** 045202
[44] Sheng X L, Yu Z M, Yu R, Weng H and Yang S A 2017 *J. Phys. Chem. Lett.* **8** 3506
[45] Yang H, Yu J, Parkin S S P, Felser C, Liu C X and Yan B 2017 *Phys. Rev. Lett.* **119** 136401
[46] Teo J C Y, Fu L and Kane C L 2008 *Phys. Rev. B* **78** 045426
[47] Heyd J, Scuseria G E and Ernzerhof M 2003 *J. Chem. Phys.* **118** 8207
[48] Wu Q, Zhang S, Song H F, Troyer M and Soluyanov A A 2018 *Comput. Phys. Commun.* **224** 405
[49] Yu J, Yan B and Liu C X 2017 *Phys. Rev. B* **95** 235158
[50] Liu C, Lee Y, Kondo T, Mun E D, Caudle M, Harmon B N, Bud'ko S L, Canfield P C and Kaminski A 2011 *Phys. Rev. B* **83** 205133
[51] Liu Z K, Yang L X, Wu S C, Shekhar C, Jiang J, Yang H F, Zhang Y, Mo S K, Hussain Z, Yan B, Felser C and Chen Y L 2016 *Nat. Commun.* **7** 12924
[52] Stringfellow G B and Chen G S 1991 *J. Vac. Sci. & Technol. B* **9** 2182
[53] Cripps S, Hosea T, Krier A, Smirnov V, Batty P, Zhuang Q, Lin H, Liu P and Tsai G 2008 *Thin Solid Films* **516** 8049
[54] Svensson S P, Sarney W L, Hier H, Lin Y, Wang D, Donetsky D, Shterengas L, Kipshidze G and Belenky G 2012 *Phys. Rev. B* **86** 245205
[55] Suchalkin S, Ludwig J, Belenky G, Laikhtman B, Kipshidze G, Lin Y, Shterengas L, Smirnov D, Luryi S, Sarney W and Svensson S P 2016 *J. Phys. D: Appl. Phys.* **49** 105101
[56] Jen H R, Ma K Y and Stringfellow G B 1989 *Appl. Phys. Lett.* **54** 1154
[57] Kurtz S R, Dawson L R, Biefeld R M, Follstaedt D M and Doyle B L 1992 *Phys. Rev. B* **46** 1909
[58] Wei S and Zunger A 1991 *Appl. Phys. Lett.* **58** 2684
[59] Belenky G, Lin Y, Shterengas L, Donetsky D, Kipshidze G and Suchalkin S 2015 *Electron. Lett.* **51** 1521
[60] Ivanov D A 2001 *Phys. Rev. Lett.* **86** 268
[61] Read N and Green D 2000 *Phys. Rev. B* **61** 10267
[62] Kitaev A Y 2001 *Physics-Uspekhi* **44** 131
[63] Kitaev A 2003 *Ann. Phys.* **303** 2
[64] Nayak C, Simon S H, Stern A, Freedman M and Das Sarma S 2008 *Rev. Mod. Phys.* **80** 1083
[65] Lutchyn R M, Sau J D and Das Sarma S 2010 *Phys. Rev. Lett.* **105** 077001
[66] Oreg Y, Refael G and von Oppen F 2010 *Phys. Rev. Lett.* **105** 177002
[67] Das A, Ronen Y, Most Y, Oreg Y, Heiblum M and Shtrikman H 2012 *Nat. Phys.* **8** 887
[68] Deng M T, Yu C L, Huang G Y, Larsson M, Caroff P and Xu H Q 2012 *Nano Lett.* **12** 6414
[69] Mourik V, Zuo K, Frolov S M, Plissard S R, Bakkers E P A M and Kouwenhoven L P 2012 *Science* **336** 1003
[70] Albrecht S M, Higginbotham A P, Madsen M, Kuemmeth F, Jespersen T S, Nygård J, Krogstrup P and Marcus C M 2016 *Nature* **531** 206
[71] Zhang H, Gül Ö, Conesa-Boj S, Zuo K, Mourik V, de Vries F K, van Veen J, van Woerkom D J, Nowak M P, Wimmer M, Car D, Plissard S, Bakkers E P A M, Quintero-Pérez M, Goswami S, Watanabe K, Taniguchi T and Kouwenhoven L P 2016 *Nature Nanotechnology*
[72] Yu R, Qi X L, Bernevig A, Fang Z and Dai X 2011 *Phys. Rev. B* **84** 075119
[73] Sgiarovello C, Peressi M and Resta R 2001 *Phys. Rev. B* **64** 115202
[74] Fu L and Kane C L 2006 *Phys. Rev. B* **74** 195312
[75] Soluyanov A A and Vanderbilt D 2011 *Phys. Rev. B* **83** 235401
[76] Gresch D, Autès G, Yazyev O V, Troyer M, Vanderbilt D, Bernevig B A and Soluyanov A A 2017 *Phys. Rev. B* **95** 075146
[77] Fang C, Gilbert M J and Bernevig B A 2012 *Phys. Rev. B* **86** 115112
[78] Soluyanov A A and Vanderbilt D 2012 *Phys. Rev. B* **85** 115415
[79] Ezawa M 2017 *Phys. Rev. B* **95** 205201
[80] Sengupta P, Ryu H, Lee S and Tan Y 2014 arXiv:1409.4376
[81] Sancho M P L, Sancho J M L and Rubio J 1984 *J. Phys. F: Met. Phys.* **14** 1205
[82] Sancho M P L, Sancho J M L and Rubio J 1985 *J. Phys. F: Met. Phys.* **15** 851
[83] Adler S L 1969 *Phys. Rev.* **177** 2426
[84] Bell J S and Jackiw R 1969 *Il Nuovo Cimento A (1971-1996)* **60** 47
[85] Nielsen H and Ninomiya M 1983 *Phys. Lett. B* **130** 389
[86] Hosur P and Qi X 2013 *C. R. Phys.* **14** 857
[87] Son D T and Spivak B Z 2013 *Phys. Rev. B* **88** 104412
[88] Abrikosov A A 1998 *Phys. Rev. B* **58** 2788
[89] Mikitik G P and Sharlai Y V 1999 *Phys. Rev. Lett.* **82** 2147
[90] Kim H J, Kim K S, Wang J F, Sasaki M, Satoh N, Ohnishi A, Kitaura M, Yang M and Li L 2013 *Phys. Rev. Lett.* **111** 246603
[91] Hirschberger M, Kushwaha S, Wang Z, Gibson Q, Liang S, Belvin C A, Bernevig B A, Cava R J and Ong N P 2016 *Nat. Mater.* **15** 1161
[92] Arnold F, Shekhar C, Wu S C, Sun Y, dos Reis R D, Kumar N, Naumann M, Ajeesh M O, Schmidt M, Grushin A G, Bardarson J H, Baenitz M, Sokolov D, Borrmann H, Nicklas M, Felser C, Hassinger E and Yan B 2016 *Nat. Commun.* **7** 11615
[93] Hu J, Xu S Y, Ni N and Mao Z 2019 *Annu. Rev. Mater. Res.* **49** annurev-matsci-070218-010023
[94] Lu H Z and Shen S Q 2017 *Front. Phys.* **12** 127201
[95] Jia S, Xu S Y and Hasan M Z 2016 *Nat. Mater.* **15** 1140
[96] Li Z, Zeng Y, Zhang J, Zhou M and Wu W 2018 *Phys. Rev. B* **98** 165441
[97] Huang X, Zhao L, Long Y, Wang P, Chen D, Yang Z, Liang H, Xue M, Weng H, Fang Z, Dai X and Chen G 2015 *Phys. Rev. X* **5** 031023
[98] Liang S, Lin J, Kushwaha S, Xing J, Ni N, Cava R J and Ong N P 2018 *Phys. Rev. X* **8** 031002
[99] Ghimire N J, Luo Y, Neupane M, Williams D J, Bauer E D and Ronning F 2015 *J. Phys.: Condens. Matter* **27** 152201
[100] Singha R, Pariari A K, Satpati B and Mandal P 2017 *Proc. Natl. Acad. Sci.* **114** 2468
[101] Du J, Wang H, Chen Q, Mao Q, Khan R, Xu B, Zhou Y, Zhang Y, Yang J, Chen B, Feng C and Fang M 2016 *Sci. Chin. Phys. Mech. & Astron.* **59** 657406
[102] Mangelsen S, Naumov P G, Barkalov O I, Medvedev S A, Schnelle W, Bobnar M, Mankovsky S, Polesya S, Näther C, Ebert H and Bensch W 2017 *Phys. Rev. B* **96** 205148
[103] Zhang C, Guo C, Lu H, Zhang X, Yuan Z, Lin Z, Wang J and Jia S 2015 *Phys. Rev. B* **92** 041203
[104] Thirupathaiah S, Jha R, Pal B, Matias J S, Das P K, Sivakumar P K, Vobornik I, Plumb N C, Shi M, Ribeiro R A and Sarma D D 2017 *Phys. Rev. B* **95** 241105
[105] Wang A, Graf D, Liu Y, Du Q, Zheng J, Lei H and Petrovic C 2017 *Phys. Rev. B* **96** 121107
[106] Zhu Z, Lin X, Liu J, Fauqué B, Tao Q, Yang C, Shi Y and Behnia K 2015 *Phys. Rev. Lett.* **114** 176601
[107] Pariari A, Singha R, Roy S, Satpati B and Mandal P 2018 *Sci. Rep.* **8** 10527
[108] Zhao Y, Liu H, Yan J, An W, Liu J, Zhang X, Wang H, Liu Y, Jiang H, Li Q, Wang Y, Li X Z, Mandrus D, Xie X C, Pan M and Wang J 2015 *Phys. Rev. B* **92** 041104
[109] Sharma G, Goswami P and Tewari S 2017 *Phys. Rev. B* **96** 045112

[110] Wang Y, Liu E, Liu H, Pan Y, Zhang L, Zeng J, Fu Y, Wang M, Xu K, Huang Z, Wang Z, Lu H Z, Xing D, Wang B, Wan X and Miao F 2016 *Nat. Commun.* **7** 13142

[111] Jeon S, Zhou B B, Gyenis A, Feldman B E, Kimchi I, Potter A C, Gibson Q D, Cava R J, Vishwanath A and Yazdani A 2014 *Nat. Mater.* **13** 851

[112] Burkov A A and Kim Y B 2016 *Phys. Rev. Lett.* **117** 136602

[113] Xu X T and Jia S 2016 *Chin. Phys. B* **25** 117204

[114] Lifshits E and Kosevich A 1958 *J. Phys. Chem. Solids* **4** 1

[115] Sun H P and Lu H Z 2019 *Front. Phys.* **14** 33405

[116] Zhang Y, Tan Y W, Stormer H L and Kim P 2005 *Nature* **438** 201

[117] Xiao D, Chang M C and Niu Q 2010 *Rev. Mod. Phys.* **82** 1959

[118] Wang C M, Lu H Z and Shen S Q 2016 *Phys. Rev. Lett.* **117** 077201

[119] Murakawa H, Bahramy M S, Tokunaga M, Kohama Y, Bell C, Kaneko Y, Nagaosa N, Hwang H Y and Tokura Y 2013 *Science* **342** 1490

[120] Fang C, Chen Y, Kee H Y and Fu L 2015 *Phys. Rev. B* **92** 081201

[121] Kane C L and Lubensky T C 2014 *Nat. Phys.* **10** 39

[122] Stenull O, Kane C L and Lubensky T C 2016 *Phys. Rev. Lett.* **117** 068001

[123] Süsstrunk R and Huber S D 2015 *Science* **349** 47

[124] Süsstrunk R and Huber S D 2016 *Proc. Natl. Acad. Sci.* **113** E4767

[125] Huber S D 2016 *Nat. Phys.* **12** 621

[126] Zhang T, Song Z, Alexandradinata A, Weng H, Fang C, Lu L and Fang Z 2018 *Phys. Rev. Lett.* **120** 016401

[127] Esmann M, Lamberti F R, Senellart P, Favero I, Krebs O, Lanco L, Gomez Carbonell C, Lemaître A and Lanzillotti-Kimura N D 2018 *Phys. Rev. B* **97** 155422

[128] Li J, Xie Q, Ullah S, Li R, Ma H, Li D, Li Y and Chen X Q 2018 *Phys. Rev. B* **97** 054305

[129] Xie Q, Li J, Liu M, Wang L, Li D, Li Y and Chen X Q 2018 arXiv:1801.04048

[130] Miao H, Zhang T T, Wang L, Meyers D, Said A H, Wang Y L, Shi Y G, Weng H M, Fang Z and Dean M P M 2018 *Phys. Rev. Lett.* **121** 035302

[131] Zhang L, Ren J, Wang J S and Li B 2010 *Phys. Rev. Lett.* **105** 225901

[132] Zhang L and Niu Q 2015 *Phys. Rev. Lett.* **115** 115502

[133] Wang P, Lu L and Bertoldi K 2015 *Phys. Rev. Lett.* **115** 104302

[134] Lu J, Qiu C, Ye L, Fan X, Ke M, Zhang F and Liu Z 2017 *Nat. Phys.* **13** 369

[135] Fleury R, Khanikaev A B and Alù A 2016 *Nat. Commun.* **7** 11744

[136] Peng Y G, Qin C Z, Zhao D G, Shen Y X, Xu X Y, Bao M, Jia H and Zhu X F 2016 *Nat. Commun.* **7** 13368

[137] Liu Y, Lian C S, Li Y, Xu Y and Duan W 2017 *Phys. Rev. Lett.* **119** 255901

[138] Liu Y, Xu Y, Zhang S C and Duan W 2017 *Phys. Rev. B* **96** 064106

[139] Liu Y, Xu Y and Duan W 2018 *Natl. Sci. Rev.* **5** 314

[140] Jin Y, Wang R and Xu H 2018 *Nano Lett.* **18** 7755

[141] Zhang X, Xiao M, Cheng Y, Lu M H and Christensen J 2018 *Commun. Phys.* **1** 97

[142] Raghu S and Haldane F D M 2008 *Phys. Rev. A* **78** 033834

[143] Mei J, Wu Y, Chan C T and Zhang Z Q 2012 *Phys. Rev. B* **86** 035141

[144] Sun K, Liu W V, Hemmerich A and Das Sarma S 2012 *Nat. Phys.* **8** 67

[145] Khanikaev A B, Hossein Mousavi S, Tse W K, Kargarian M, MacDonald A H and Shvets G 2013 *Nat. Mater.* **12** 233

[146] Lu L, Fu L, Joannopoulos J D and Soljacic M 2013 *Nat. Photon.* **7** 294

[147] Rechtsman M C, Plotnik Y, Zeuner J M, Song D, Chen Z, Szameit A and Segev M 2013 *Phys. Rev. Lett.* **111** 103901

[148] Lu L, Joannopoulos J D and Soljacic M 2014 *Nat. Photon.* **8** 821

[149] He W Y and Chan C T 2015 *Sci. Reports* **5** 8186

[150] Liu S and Hou Q 2017 *J. Phys. B: At. Mol. Opt. Phys.* **50** 245001

[151] Fulga I C, Fallani L and Burrello M 2018 *Phys. Rev. B* **97** 121402

[152] Prodan E and Prodan C 2009 *Phys. Rev. Lett.* **103** 248101

[153] Snyder G J and Toberer E S 2008 *Nat. Mater.* **7** 105

[154] Rowe D M 2005 *Thermoelectrics handbook: macro to nano* (CRC press)

[155] Zhao L D, Lo S H, Zhang Y, Sun H, Tan G, Uher C, Wolverton C, Dravid V P and Kanatzidis M G 2014 *Nature* **508** 373

[156] Duong A T, Nguyen V Q, Duvjir G, Duong V T, Kwon S, Song J Y, Lee J K, Lee J E, Park S, Min T, Lee J, Kim J and Cho S 2016 *Nat. Commun.* **7** 13713

[157] Zhao L D, Tan G, Hao S, He J, Pei Y, Chi H, Wang H, Gong S, Xu H, Dravid V P, Uher C, Snyder G J, Wolverton C and Kanatzidis M G 2016 *Science* **351** 141

[158] Singh S, Ibarra-Hernandez W, Valencia-Jaime I, Avendano-Franco G and Romero A H 2016 *Phys. Chem. Chem. Phys.* **18** 29771

[159] Terasaki I, Sasago Y and Uchinokura K 1997 *Phys. Rev. B* **56** R12685

[160] Takahata K, Iguchi Y, Tanaka D, Itoh T and Terasaki I 2000 *Phys. Rev. B* **61** 12551

[161] Okuda T, Nakanishi K, Miyasaka S and Tokura Y 2001 *Phys. Rev. B* **63** 113104

[162] Mahan G D and Sofo J O 1996 *Proc. Natl. Acad. Sci.* **93** 7436